1 **Co-ZIF reinforced cow manure biochar (CMB) as an effective**

2 **peroxymonosulfate activator for degradation of carbamazepine**

3 Yongxin Lei[1,2‡], Xiao Guo[1‡], Mingjie Jiang[1*], Wen Sun[1], Huan He[2], Yu Chen[3], Kunyapat

4 Thummavichai[2,4], Oluwafunmilola Ola[5], Yanqiu Zhu[1,2,3*], Nannan Wang[1,2*]

5

6 [1] Key Laboratory of Disaster Prevention and Structural Safety of Ministry of Education,

7 Guangxi Key Laboratory of Disaster Prevention and Engineering Safety, Guangxi

8 University, Nanning, 530004, China

9 [2]Guangxi Institute Fullerene Technology (GIFT), Key Laboratory of New Processing

10 Technology for Nonferrous Metals and Materials, Ministry of Education, School of

11 Resources, Environment and Materials, Guangxi University, Nanning, 530004, China

12 [3] College of Engineering, Mathematics and Physical Sciences, University of Exeter,

13 Exeter, EX4 4QF, UK

14 [4] Department of Mathematics, Physics and Electrical Engineering, Faculty of

15 Engineering and Environment, Northumbria University, NE1 8ST, UK

16 [5] Advanced Materials Group, Faculty of Engineering, The University of Nottingham,

17 Nottingham, NG7 2RD, UK

18 [‡] These authors contributed equally.

19 *Corresponding author: Mingjie Jiang, Nannan Wang, Yanqiu Zhu.*

20 E-mail: *jiangmingjie@gxu.edu.cn, wangnannan@gxu.edu.cn, Y.zhu@exeter.ac.uk*

21

Abstract:

Excessive emissions of cow manure have put tremendous pressure on environment, the difficulties in disposal methods have presented serious challenges to the livestock industry. Herein, cow manure biochar (CMB) loaded metal-organic framework (ZIF-67) precursors derived Co nanoparticles carbon (Co@NPC) at different temperatures to form biochar-based composites, *i.e.*, Co@NPC-CMB-x. The novel non-homogeneous catalysts activated peroxymonosulfate (PMS) to degrade the carbamazepine (CBZ). The results demonstrated that the pyrolysis temperature directly influenced the intrinsic properties and catalytic ability of products, with the higher pyrolysis temperature favoring the conversion of more graphitic C and graphitic N as active sites. In particular, Co@NPC-CMB-800 showed excellent activation of PMS, degrading 100% CBZ within 30 min. The high specific surface area, highly graphitic structure and the uniform dispersion of cobalt species were the key reasons for the excellent catalytic ability. X-ray photoelectron spectroscopy (XPS) illustrated that the interaction between biochar and transition metal was responsible to generate more reactive oxygen species. Furthermore, electron paramagnetic resonance (EPR) confirmed that non-radical singlet oxygen is the dominant pathway for CBZ degradation by the catalyst. This study provides a new strategy for cow manure application in functional catalysts and offers new prospects for designing efficient biochar-based catalysts for environmental remediation.

Keywords:

Cow manure, Zeolitic imidazolate frameworks, Peroxymonosulfate (PMS) Oxidation.

1.Introduction

The transformation of biomass materials into sustainable end-products in order to achieve a circular bioeconomy has attracted a considerable amount of attention [1]. Biochar (BC), a carbon-based material produced by pyrolysis [2], hydrothermal carbonization [3] or gasification [4] of biomass raw materials under anaerobic or oxygen-limited conditions [5, 6]. It has been effectively used in applications such as soil amendment [7], adsorbent [8], wastewater treatment [9] and carbon sequestration [10] due to its excellent physicochemical properties like wide source, large specific surface area, biodegradable and rich in oxygen-containing functional groups [11-13]. Previously, biochar was primarily derived from agricultural waste or wood processing waste. However, fewer studies have been carried out with biochar derived from animal manure [2]. As the number of cows increases, the contamination caused by cow manure carrying pathogens will cause serious environmental and public health problems [14]. Therefore, the rational application of cow manure is considered as one of the great challenges faced by the livestock industry. We believe that the preparation of biochar from raw materials of cow manure is an efficient strategy for the effective reusing of pollutants in animal husbandry, providing a new way for recycling and reusing cow manure.

Carbamazepine (CBZ), one of the most commonly used pharmaceutical and personal care products (PPCP), is used to treat bipolar disorder, epilepsy, and trigeminal neuralgia [15, 16]. However, CBZ cannot be totally absorbed by human body or natural environment because the olefinic double bond on the central heterocyclic ring of CBZ makes itself difficult to degrade [17, 18]. These residues, produced by pharmaceutical companies and difficult to absorb after ingestion, can hardly be degraded. The usual treatment is to discharge the waste into the aqueous environment, which has toxic effects on the ecosystem [19, 20]. Therefore, it is becoming increasingly urgent to develop technologies for the effective removal of CBZ. Dong et al. successfully eliminated antibiotic biotoxicity after photocatalytic degradation by preparing a double

74   Z-scheme mechanism with visible light-responsive tetradecahedral ZnO-SnO_2-

75   Zn_2SnO_4 catalyst [21]. Xiong and co-workers prepared reduced graphene oxide

76   modified black scale quantum dots to promote photogenerated carrier spatial separation

77   via the formation of n-n type high-low junctions and internal electric fields based on

78   different Fermi energy levels [22]. Furthermore, Wei's group designed TiO_2@$LaFeO_3$

79   nanospheres with hollow core-shell architecture to remove the persistent pollutant

80   atrazine by enhanced electron transfer [23]. Among these new pollutant treatment

81   methods, the Advanced Oxidation Process (AOPs), a pollutant treatment method based

82   on reactive oxygen species (ROS) such as sulfate ($SO_4^{\bullet-}$) and hydroxyl radicals ($OH^{\bullet}$),

83   can achieve complete degradation of organic contaminants by mineralizing toxic and

84   hard-to-degrade pollutants into small molecules [24-26]. However, compare with $OH^{\bullet}$

85   which has the disadvantages of pH limitation and extremely short half-life (<1 μs), $SO_4^{\bullet-}$

86   possesses a higher redox potential ($SO_4^{\bullet-}$, 2.5-3.1 V, $OH^{\bullet}$, 1.9-2.7 V) that can be

87   produced more efficiently over a wider pH range and persists longer in aqueous

88   solutions [27-29]. Therefore, sulfate radical-based advanced oxidation processes (SR-

89   AOPs) has grown in popularity in the application of removing organic pollutants from

90   water. The most common method to obtain $SO_4^{\bullet-}$ is to activate persulfate (PDS and PMS)

91   with light, heat, transition metals, etc. [30-32] Among them, transition metals exhibit

92   outstanding catalytic performance, and cobalt ions have been reported to be the most

93   effective transition metal for activating PMS [33].

94   Metal-organic frameworks (MOFs) are porous coordination polymers formed by

95   the self-assembly of metal cluster linkage nodes and organic ligands [34]. Since their

96   emergence, MOFs have received widespread attention in the fields of catalysis [35],

97   chemical sensing [36], energy storage and conversion [37], drug delivery [38] and so

98   on. Zeolitic imidazolate frameworks (ZIFs), a subclass of MOFs, consist of cobalt or

99   zinc as metal nodes and imidazolate as organic ligands [39-41]. Since its emergence,

100 ZIF-67 has received considerable attention in the field of catalysis in recent years [42].

101 Among these, N-doped porous hybrid materials derived from ZIF-67 showed promising

102   candidates for use in SR-AOPs [43]. The Co-Nx group which served as active sites can

103   be generated by 2-methylimidazole as nitrogen source under pyrolytic conditions [44].

104   Moreover, previous studies discovered that the ZIF-derived metallic carbon catalysts

105   effectively inhibit the leaching of transition metals. Because the majority of the metal

106   particles were covered by carbon shells, reducing contact between the metal particles

107   and the H^+ in solution environment [45, 46]. However, the aggregate tendency of metal

108   nanoparticles formed by pyrolysis, which affected the catalytic effect, remained a

109   challenge to improve [47]. Some research has concluded that the development of

110   suitable support substrates can lead to uniformly dispersed and size-controlled Co-

111   based catalysts [48]. Hu and co-workers designed to grow MOFs-derived layered

112   hydroxides on MXene, creating new active sites in the process of accelerating charge

113   transport [49]. Ye et al. grew ZIF-67 in situ on g-C_3N_4 to generate carbon nanotube

114   composites by pyrolysis, which showed excellent performance in activating PMS for

115   sulfamethoxazole degradation [44]. Xu et al. proposed pyrolysis of wheat straw to

116   generate BC that was loaded with Co_3O_4 fabricated by ZIF-67, and the synthesized

117   composites significantly enhanced the dispersibility of Co_3O_4/C nanoparticles [50]. As

118   the functional groups on the surface of BC can interact with metal, it could improve the

119   dispersion and stability of metal nanoparticles within the substrates [51, 52]. It is a

120   promising strategy to apply modified biochar to SR-AOPs that can effectively improve

121   the application of BC and cobalt-based materials. Few papers, however, have

122   thoroughly investigated the effect of pyrolysis temperature on the catalyst synthesized

123   from BC and ZIF precursors and its ability to activate PMS.

124   In this paper, cow manure and ZIF-67 were chosen as dual-precursor to prepare

125   Co@NPC-CMB-x magnetic composites using a simple pyrolysis method as the non-

126   homogeneous catalyst to activate PMS to degrade CBZ. Further investigated the effect

127   of different pyrolysis temperatures on the intrinsic properties and catalytic

128   performances of composites in detail. It was found that the increase in pyrolysis

129   temperature significantly increased the number of active groups of catalysts, including

130 crystallinity, specific surface area and graphite degree which effectively improve the

131 catalytic properties. ZIF-67 as the self-sacrificing template provided plentiful nitrogen

132 sources, and the interaction of BC and transition metals promoted electron transfer

133 during the reaction. The degradation performance of CBZ was probed under various

134 catalytic conditions (catalyst dosage, PMS dosage, initial pH, initial CBZ concentration,

135 catalytic temperature, inorganic anion). Moreover, the mechanisms of catalytic process

136 were explored and concluded by XPS, EPR and radical-quenching experiments. The

137 purpose of this study was to convert cow manure from the livestock industry waste into

138 materials for water pollution treatment and to provide examples for biochar application
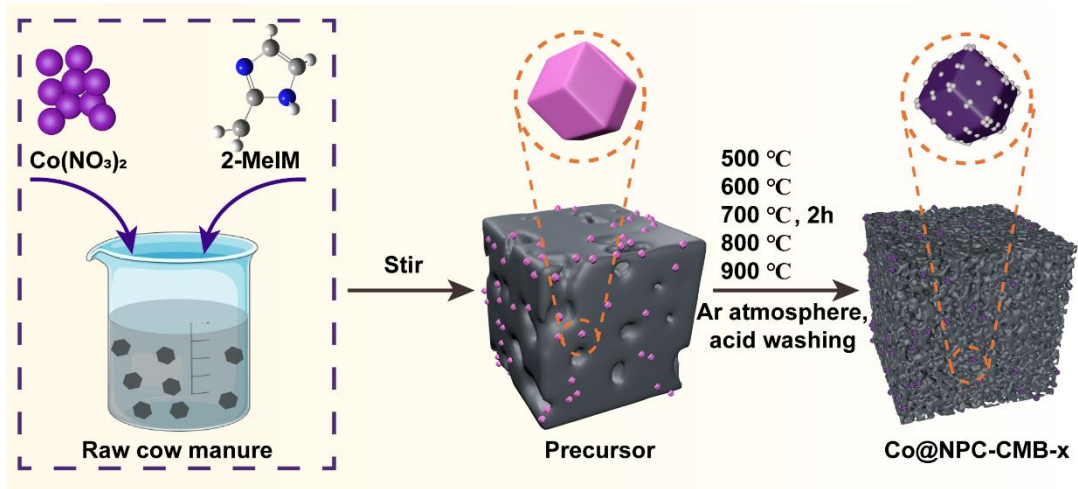
139 in SR-AOPs.

2. Experimental

2.1. Chemical Reagents

The raw cow manure was obtained from a dairy farm in Guangxi. Cobalt nitrate hexahydrate $(Co(NO_3)_2 \cdot 6H_2O$, 99%), 2-methylimidazole (2-MeIM), anhydrous methanol (MeOH), sodium hydroxide (NaOH), *tert*-butanol (TBA), L-Histidine, p-Benzoquinone (PBQ), sodium thiosulfate $(Na_2S_2O_3 \cdot 5H_2O)$, were purchased from Sinopharm Chemical Reagent Co., Ltd.; Model pollutant carbamazepine (CBZ), 5,5-dimethyl-1-pyrroline N-oxide (DMPO), 2,2,6,6-Tetramethyl-4-piperidone(TEMP), and potassium peroxymonosulfate (PMS, $KHSO_5 \cdot 0.5KHSO_4 \cdot 0.5K_2SO_4$) were obtained from Macklin. All the materials used in this study were of analytical grade and used as received without further purification. Deionized water was applied in all the experiments.

2.2. Synthesis of Catalysts

The schematic of the Co@NPC-CMB synthesis process was illustrated in Fig. 1. Firstly, the collected cow manure was grounded in small size, rinsed with deionized water and dried at 60 °C for subsequent use. Secondly, 2 g of dried cow manure and 3 mmol of cobalt nitrate hexahydrate were mixed into 90 mL of methanol and stirred continuously for two hours as solution A and cobalt ions attached to the surface of cow manure by chelation. 24 mmol of 2-MeIM dissolved in methanol solution named solution B. Then solution A was poured into solution B rapidly and stirred vigorously for 10 min, left to stand for 24 h at room temperature. The product was washed three times with methanol and dried at 60 °C in the oven. Thirdly, the dried samples were placed in a quartz boat and placed in a tube furnace under Ar atmosphere to pyrolyze at 500, 600, 700, 800 and 900 °C for 2 h (heating rate was 2 °C/min). After cooling down, the product was impregnated in 3 M HCl to remove excess Co species and reduce cobalt leaching. The samples synthesized at different pyrolysis temperatures from 500 °C to 900 °C were named Co@NPC-CMB-x (x=500, 600, 700, 800 and 900). The cow manure and ZIF-67 precursors pyrolyzed at 800 °C under the same atmosphere were

168   named CMB and Co@NPC, respectively.

2.3. Catalytic Activity Measurements

The degradation experiments were carried out in a 250 mL beaker at 25 °C. CBZ was dissolved in deionized water and heated to 60 °C until the powder was completely dissolved. Then the solution was fixed in a volumetric flask and continued to stir for 12 hours to obtain CBZ solution with a concentration of 15 mg/L and an initial pH of 6.8. In a typical experiment, a predetermined dosage of PMS was added to the CBZ solution and stirred for 5 min to allow complete dispersion of PMS without pH adjustment. Subsequently, a certain amount of catalyst was added. The reaction solution (1 mL) was withdrawn and injected into $Na_2S_2O_3$ (50 μL) solution at regular intervals to scavenge free radicals and prevent further reactions. The extracted reaction solution was filtered through 0.22 μm polytetrafluoroethylene filter and then analyzed by high-performance liquid chromatography (HPLC). The catalytic efficiency was Ct/Co (Ct: concentration of the reaction CBZ at t min, Co: initial CBZ concentration, t: degradation reaction time (min)). The degradation of CBZ for all kinetic experiments under different factors conformed to the pseudo-first-order kinetic equation $-ln\,(C_t\,/\,C_0) = k_{obs}{\cdot}t$, where k_{obs} is the apparent rate constant (min^{-1}). All experiments were performed in three replicates, and the experimental results were expressed as mean and standard deviation.

2.4. Material Characterizations

189   The concentration of CBZ was determined by high-performance liquid
190   chromatography (Thermo, USA) with the Acclaim 120 C18 (250 × 4.6 nm). The
191   injection volume was 10 μL and the UV detector with a detection wavelength of 286
192   nm. The mobile phase was water and acetonitrile with a volume ratio of 40:60 (v/v), a
193   flow rate of 1 mL/min, and a column temperature of 35 °C. The concentration of PMS
194   remaining in the reaction solution was determined by KI iodometric titration method
195   [53]. To exclude the effect of inorganic anions on the experiment, the pH of the solution
196   was adjusted using H_2SO_4 and NaOH, and the pH of the solution was determined using
197   the PHS-3E pH meter (Rex, China).

198   The composition of the catalyst was analyzed by X-ray diffraction (XRD, Rigaku
199   D/MAX 2500V, Japan) with Cu Kα radiation (100 mA, 40 kV) at a scanning rate of 5°
200   min^{-1}. Raman Spectral was detected by inVia Reflex (Renishaw, England). The surface
201   morphologies of catalysts were studied by field emission scanning electron microscopy
202   (FESEM, Hitachi S-4800, Japan) and high-resolution transmission electron microscopy
203   (HRTEM, FEI Tecnai G2 F20, USA). Free radicals in the system were detected by
204   electron paramagnetic resonance (EPR, Bruker A300, Germany) with a modulation
205   amplitude of 3G, microwave power of 20.00 mW, microwave frequency of 9.79 GHz,
206   and modulation frequency of 100 kHz. The elemental composition and valence states
207   of the material were analyzed by X-ray photoelectron spectroscopy (XPS, Axis Ultra
208   DLD, England). Al Kα was used as the radiation source. The measurement range was
209   from 0 eV to 1380 eV. After the degradation experiment, the cobalt element was
210   analyzed by inductively coupled plasma atomic emission spectrometry (ICP-MS, ICPS-
211   7510, Japan). The total organic carbon (TOC) was analyzed by TOC-L CSH Elementar
212   liquid TOC analyzer (Shimadzu, Japan).

## 3. Results and Discussion

3.1 Characterizations of catalyst
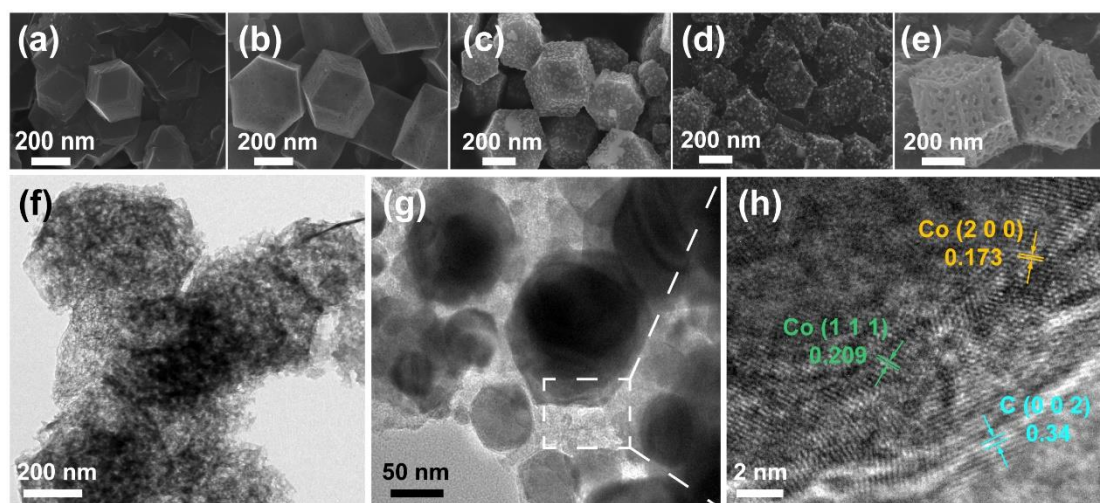
Fig. 2. SEM images of (a-e) Co@NPC-CMB-x synthesized at different pyrolysis temperatures (x=500, 600, 700, 800, 900). TEM images of (f, g) Co@NPC-CMB-800 and (h) HRTEM of Co@NPC-CMB-800.

The morphologies and microstructures of CMB, Co@NPC and Co@NPC-CMB-x were analyzed using SEM and TEM. According to Fig. S1a, the surface of raw cow manure was smooth and filled with folds in the shape of ridges. These folds increased the contact area and improved the dispersion of ZIF-67 nanoparticles on the surface of substrate. In Fig. 2(a-e), the morphology of samples prepared at different temperatures showed differences, but the hexahedral skeleton of the ZIF-67 precursor remained intact (Fig. S1b). It was observed that when the pyrolysis temperature rose from 500 °C to 600 °C, the pore size of the composite surface gradually increased. As the temperature reached 700 °C, the cobalt nanoparticles commenced precipitating. When the pyrolysis temperature was raised to 800 °C, it was found that uniform size cobalt nanoparticles (~ 30 nm) and abundant pores were distributed on the catalyst surface. Interestingly, Co@NPC-CMB-900 has coarse porous structures and further merges into rough pore networks. The increase in temperature did not result in good thermal stability. In contrast, the higher temperature led to slight cracks on the surface instead of a smooth surface. Furthermore, distinguished from Co@NPC (Fig. S1c), the Co nanoparticles in

234 Co@NPC-CMB-x were uniformly distributed without significant agglomeration

235 caused by magnetic interactions (Fig. S1d), which was attributed to the effective

236 dispersion of carbon substrate. These cobalt nanoparticles which precipitated at high

237 temperatures provided highly dense metal active sites. In addition, the diameter of the

238 pores on the ZIF surface increased further with the rising temperature. The porous

239 structure could increase the specific surface area and the larger pores provided more

240 active sites inside the catalyst. To investigate the detailed elemental composition of

241 Co@NPC-CMB-800, the energy-dispersive X-ray spectroscopy (EDX) elemental

242 mapping images were used to determine and the results were shown in Fig. S2. C, N,

243 O, and Co elements were aggregated and distributed in the catalyst, demonstrating

244 successful loading of ZIF-67 precursors on cow manure. Additionally, minor amounts

245 of Si, Mg, and Ca elements originated from biomass raw materials.

246 TEM images further demonstrated the assembly of Co species and the carbon

247 substrate, in which the hexagonal structure of ZIF-67 precursor was maintained under

248 800 °C pyrolysis condition (Fig. 2(f-g)). It can be seen that the sample retained some

249 of Co nanoparticles encapsulated by the graphitized carbon layer after acid etched.

250 Since the acidity of 3 M HCl was lower than that of the PMS solution and the protection

251 of Co by the graphite carbon layer, the leaching of Co ions would be inhibited during

252 the activation reaction [43]. The HRTEM of the sample was shown in Fig. 2h. It was

253 observed that the lattice fringes with interlayer spacing of 0.36 nm matched with the (0

254 0 2) plane of graphite carbon. Meanwhile, the interplanar spacing of 0.173 nm and

255 0.209 nm correspond to the (2 0 0) and (1 1 1) planes of Co. In summary, raw cow

256 manure was the substrate used to load ZIF-67 precursor, and the interaction resulted in

257 the homogeneous dispersion of Co species. The uniform distribution of transition metal

258 particles and the abundance of pores that appeared at higher temperatures would

259 provide more active sites, increasing the reactivity of the catalyst as pyrolysis

260 temperatures increased.
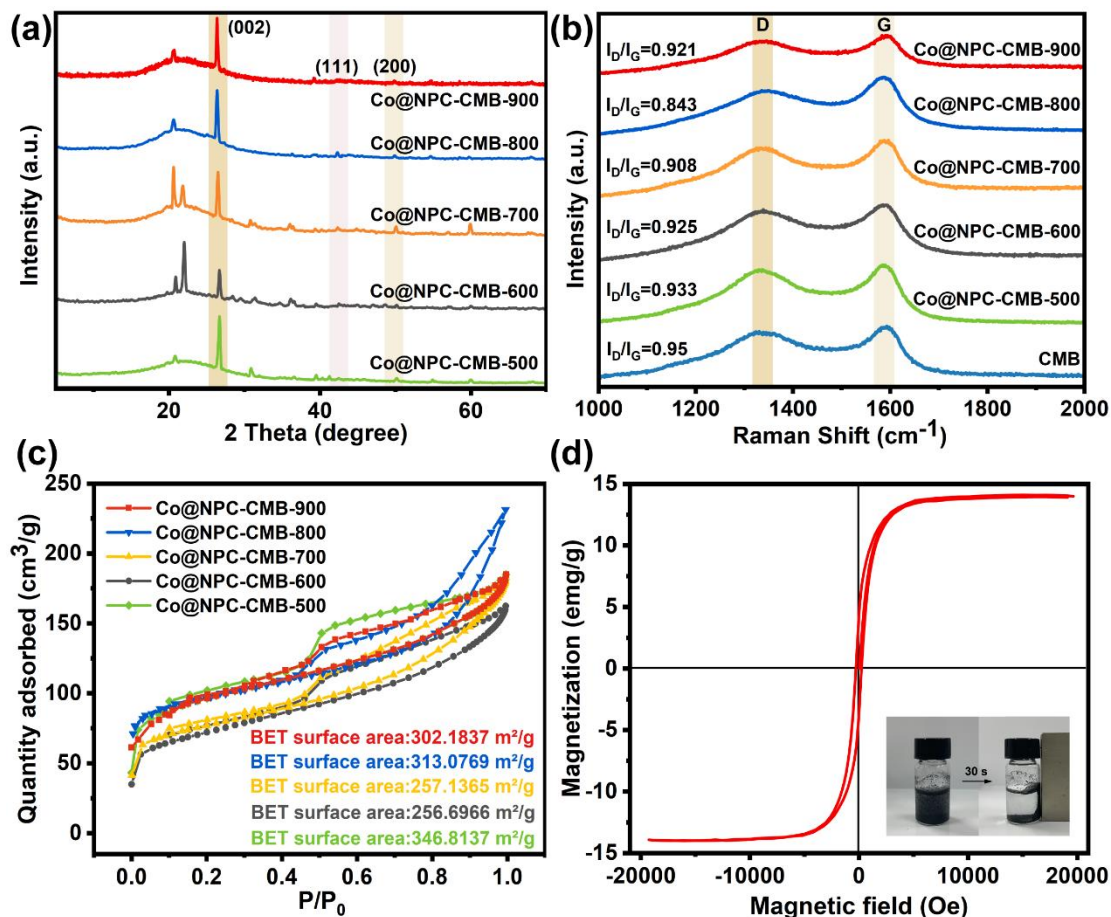
Fig. 3. (a) The XRD patterns of Co@NPC-CMB-x. (b) Raman spectra of Co@NPC-CMB-x and CMB. (c) N_2 adsorption-desorption isotherms of Co@NPC-CMB-x. (d) The magnetic hysteresis loop of Co@NPC-CMB-800. The inset showed excellent magnetic separation property of Co@NPC-CMB-800 under an external magnetic field (30 s).

The crystal phase composition of the materials was determined by XRD (Fig. 3a). For different pyrolysis temperatures, Co@NPC-CMB-x exhibited similar patterns. The most intense peak at $2\theta = 26.38°$ can be observed as the characteristic of graphitic carbon belonging to [54]. The enhanced intensity of the graphitic C diffraction peak with the increasing pyrolysis temperature, indicating that the graphitization degree was promoted at higher pyrolysis temperatures. Meanwhile, two distinctive peaks were found at 42.3° and 49.8°, which coincided with the (1 1 1) and (2 0 0) planes of the face-centered cubic Co [55, 56]. It demonstrated the successful loading of Co nanoparticles after pyrolysis. The intensity of the Co diffraction peaks in Co@NPC-CMB-x was not obvious when compared to Co@NPC (Fig. S3). The reason for this

276 might be Co nanoparticles were wrapped in biochar and graphitic layers. Meanwhile,

277 most of Co nanoparticles were etched after soaking in 3 M HCl. In addition, it could

278 observe that the intensity of the Co diffraction peaks was enhanced with the raising

279 pyrolysis temperature. This meant that increasing the pyrolysis temperature could

280 improve the crystallinity of the composites efficiently. However, the diffraction peak of

281 Co in Co@NPC-CMB-900 was not as obvious as in Co@NPC-CMB-800, which could

282 be attributed to further increases in temperature destroying the crystallinity of samples.

283 Fig. 3b was recorded to further clarify the graphitization degree of Co@NPC-

284 CMB-x by Raman spectroscopy. All samples showed two typical Raman characteristic

285 peaks at 1324 cm^{-1} and 1581 cm^{-1}, belonging to D-band and G-band [57]. The D-band

286 represented the defects/disorders of carbon-based materials, and the G-band

287 demonstrated the degree of sp^2-hybridized carbon of graphitic structure [58, 59]. The

288 degree of graphitization in the carbon layers could be compared by the band intensity

289 ratio, i.e., I_D/I_G. It was found that the I_D/I_G value of the composites decreased from 0.933

290 to 0.843 as the pyrolysis temperature increased from 500 ℃ to 800 ℃. It showed that

291 the rise of pyrolysis temperatures favored an increase in the graphitization degree.

292 Furthermore, the I_D/I_G value increased when the temperature further increased to 900 ℃.

293 This may be because the higher temperature destroyed the structure of the carbon

294 material, causing an increase in defects. And the higher degree of graphitization would

295 effectively facilitate charge transfer and improve the activation capacity aimed at PMS

296 by carbonaceous materials [60]. Moreover, it was worth noting that CMB has the

297 highest degree of disorder with the I_D/I_G value reaching 0.95 compared to those

298 materials doped with transition metals. This phenomenon indicated that the

299 incorporation of transition metal Co effectively enhanced the sp^2-hybridization of

300 carbon materials. As reported, it was considered that the change in carbon configuration

301 occurred when the amorphous Co species were transformed to metallic Co during

302 graphitization [6]. Firstly, dispersed carbon freely migrated to the surface of Co

303 nanoparticles and reconstituted into graphitic carbon under the influence of high-

temperature environments [61]. Furthermore, as the pyrolysis temperature increased, the metallic carbide intermediates such as Co_2C decomposed and formed graphitic carbon layers [62]. Overall, the Raman spectral data revealed that the carbon layer structure was highly correlated with the pyrolysis temperature and metal doping.

The N_2 adsorption-desorption isotherms of Co@NPC-CMB-x were shown in Fig. 3c. All materials exhibited typical type IV isotherms accompanied by an H-3 hysteresis loop, confirming the mesoporous structure [63]. It could find that the highest specific surface area in Co@NPC-CMB-500 might attribute to the precipitation of cobalt particles at higher temperatures blocking the material. However, the BET surface area of the materials enlarged with the pyrolysis temperature increased from 600 ℃ to 800 ℃. The reason for that might be the organic substances from raw materials decomposed at higher temperatures, exposed to larger pores and channels which magnified the specific surface area [63]. The decrease in specific surface area observed for samples synthesized at 900 ℃ could attribute to the collapse of carbon skeleton structures [64]. These factors and precipitated Co particles would expose more active sites, meanwhile increasing the contact range between catalyst and contaminant so that degradation reactions could be accelerated. Furthermore, the BET surface area of Co@NPC was lower than that of CMB and Co@NPC-CMB-800 prepared at the same pyrolysis temperature (Fig. S4). It was caused by aggregation of Co nanoparticles on the surface due to magnetic action, which blocked the pores of the catalyst. Compared to other samples, Co@NPC-CMB-800 has a higher BET surface area, larger pore volume (Table. S1) and abundant metal particles. It would improve catalytic activity by facilitating the diffusion of pollutants and PMS molecules from solutions into catalysts and accelerating electron transfer capacity [65].

The magnetic properties of Co@NPC-CMB were verified by Vibrating Sample Magnetometer (VSM) (Fig. 3d). According to the measured results, the saturation magnetization (Ms) value of the composite was 14.1 emu/g. The illustration demonstrated that Co@NPC-CMB was able to distribute uniformly in solution. As a

result of the magnetic response, the catalyst was able to completely separate from the

reaction solution in the presence of an external magnetic field. This result demonstrated

that the prepared catalysts were recyclable, and this property would simplify the

recycling process considerably.
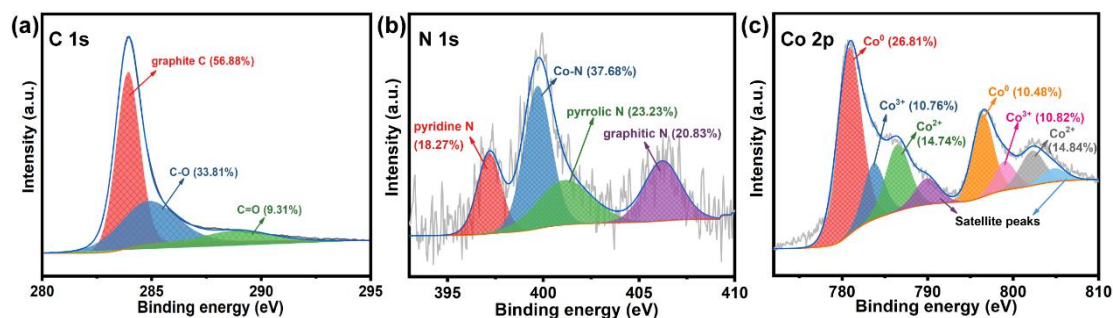
Fig. 4. XPS spectra of (a) C 1s, (b) N 1s, (c) Co 2p for Co@NPC-CMB-800.

X-ray photoelectron spectroscopy (XPS) was an effective way to understand the

elemental compositions and differences of Co@NPC-CMB-x. As shown in Fig. S5, the

full spectrum of Co@NPC-CMB-x showed characteristic peaks of C 1s, N 1s, O 1s,

and Co 2p that were consistent with the EDS results. The atomic percentages of C, N,

O, and Co were listed in Table S2. It could find that the element content of the

composites showed certain distinctions at different synthesis temperatures. As the

pyrolysis temperature increased, the total C content increased from 83.56% of

Co@NPC-CMB-500 to 84.80% of Co@NPC-CMB-800, implying that the production

of C was more favorable at higher temperatures. However, increasing the temperature

would exacerbate the thermal cracking of carbon, leading to a significant decrease in C

content, which was consistent with the BET specific surface area results. Also, the

Co@NPC-CMB-800 owned the highest Co content of 4.92%. From the above results,

the high-temperature environment favored the formation and growth of cobalt

nanoparticles and carbon precursors.

As plotted in Fig. 4a, the C 1s were deconvoluted into three peaks concentrated at

283.92 eV, 284.8 eV and 288.93 eV corresponding to graphite C, C-O, and C=O,

respectively [66]. Notably, the results in Fig. S6 showed that the increase in

carbonization temperature was accompanied by the increase of graphitic C content and

a slight drop occurred when the temperature reached 900 °C, which was consistent with the Raman results. Some reports suggested that sp^2-hybridized graphitic carbon networks were the carbon bridges that speed up the electron transfer process effetely [60]. And the high degree of graphitization would facilitate charge transfer, implying that higher pyrolysis temperature could be beneficial for the PMS activation reaction. In addition, the content of the oxygen-containing group decreased as the temperature increased. It was attributed to the destruction of oxygen-containing groups under high-temperature conditions. For N (Fig. 4b), the Co-N peak was observed in Co@NPC-CMB-x at 399.7eV corresponding to the interaction of nitrogen species with metallic cobalt [43]. In general, pyridine N in a six-membered heterocyclic ring could serve as an anchor point for the Co atom to form CoNx [67]. Thus, Co would combine with the surrounding pyridine N to formulate Co-N coordination bonds during the pyrolysis process. Meanwhile, the graphitic N content increased from 11.89% (500 °C) to 20.83% (800 °C), implying that the conversion of pyridine N and pyrrolic N to Co-N and graphite N were favored at higher temperatures (Fig. S7). As graphite N was considered to be the more efficient electron transfer nitrogen species, it could effectively enhance the activation of PMS by the catalyst [68].

For comparison of the Co species effects, the high-resolution Co 2p spectra of Co@NPC-CMB-x and ZIF-67 were investigated. As shown in Fig. 4c, two main peaks of Co 2p 3/2 and Co 2p 1/2 were located at 780.9 and 796.6 eV. And the Co 2p 3/2 region can be deconvoluted into four peaks at 779.5, 783.9, 786.6 and 790 eV for Co^0, Co^{3+}, Co^{2+} and satellite peaks, respectively. However, it was noteworthy that the fitted peak of Co^0 does not appear in the Co 2p spectrum of ZIF-67 (Fig. S9). Moreover, as observed in Fig. S8, the proportion of Co^0 got enhanced with the higher synthesis temperature, which indicated that Co^0 was generated as new active sites after high-temperature carbonization. Further calculation of the Co^{2+}/Co^{3+} atom ratio on the catalyst surface through the area covered by fitted curves (Table. S3). Obviously, Co@NPC-CMB-800 had the highest Co^{2+}/Co^{3+} atom ratio among the catalysts. It has

384   been reported that Co^{2+} was the real catalytic active center for activating PMS to

385   produce $SO_4^{\bullet-}$ [69, 70], implying that increasing the pyrolysis temperature would

386   contribute to increasing catalyst catalytic activity.

3.2 Catalytic performance of catalyst
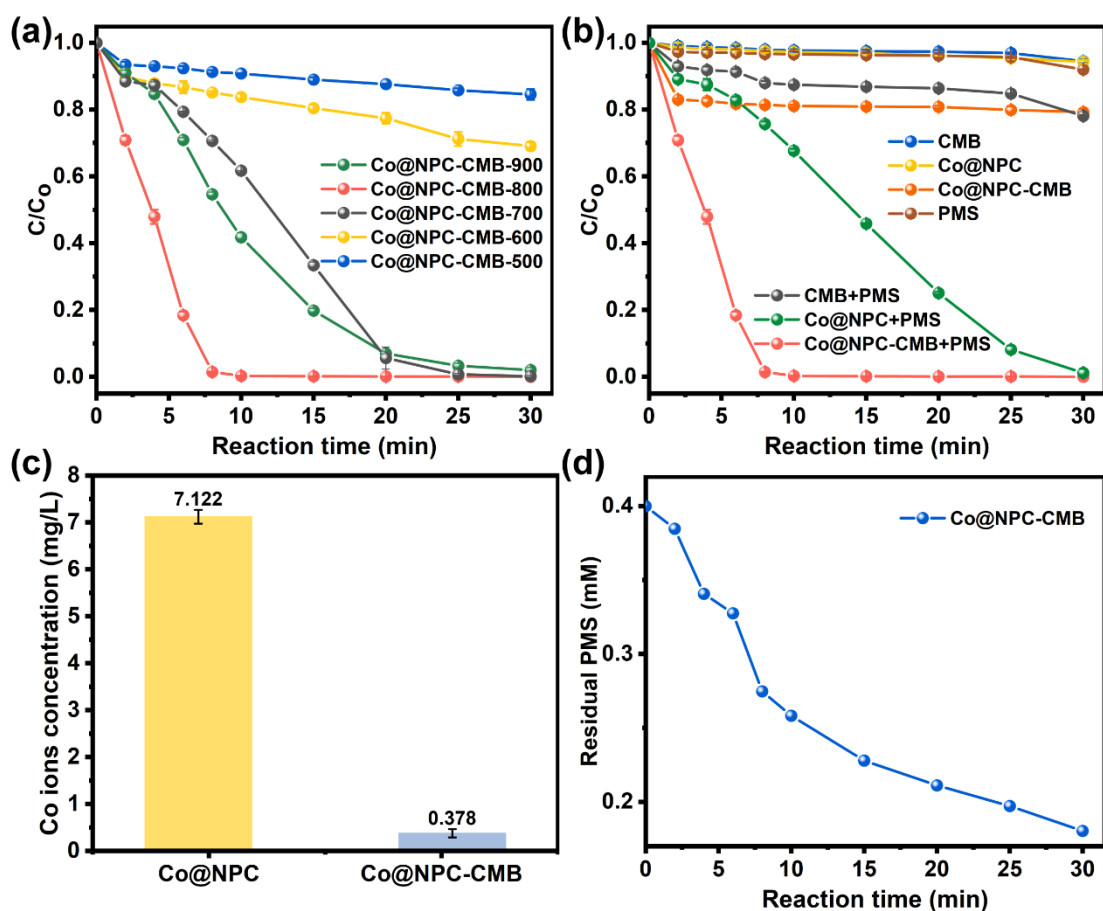
Fig. 5. (a) Degradation performance of CBZ of different composites. (b) Comparison of the CBZ degradation efficiencies in different systems. (c) Co ions concentration in different systems. (d) residual PMS. (experiment conditions: [CBZ] = 15 mg/L, [PMS] = 0.4 mM, [CMB] = 50 mg/L, [Co@NPC] = 50 mg/L, [Co@NPC-CMB-x] = 50 mg/L (x=500, 600, 700, 800 and 900), pH = 6.8, T = 25 ℃).

The pyrolysis temperature has a significant impact on the physicochemical properties of the composites, and it was meaningful to examine the effect of catalysts synthesized at different pyrolysis temperatures on the properties of PMS activation. The degradation results with the Co@NPC-CMB-x/PMS system were shown in Fig. 5a, with the catalytic performance improving significantly as the carbonization temperature increased. That was because compared to the catalysts synthesized at lower pyrolysis temperatures, Co@NPC-CMB-800 had higher crystallinity, specific surface area, and graphitization structure. In another aspect, the content of the transition metal Co increased significantly at high temperatures and provided richer metal active sites

403 (Table. S2). These properties accelerated charge transfer and mass transfer in the

404 catalyst, and increased the ability to activate PMS which accelerated the production of

405 free radicals directly. This suggested that the effect of different catalysts in the

406 Co@NPC-CMB-x system on CBZ removal was heavily influenced by their intrinsic

407 properties. Therefore, following the above facts, Co@NPC-CMB-800 was selected as

408 the most suitable catalyst condition. In the following, it was abbreviated as Co@NPC-

409 CMB.

410 The catalytic performance of different systems for the degradation of CBZ was

411 evaluated, and the results were shown in Fig. 5b. In the absence of PMS, the removal

412 of CBZ was negligible by CMB, Co@NPC and Co@NPC-CMB due to the static

413 adsorption for 5.5%, 5.7% and 20.7%, respectively, and the equilibrium state of

414 adsorption saturation was reached within half an hour. This indicated that CMB,

415 Co@NPC and Co@NPC-CMB had limitations in the removal of CBZ by adsorption.

416 Then PMS was introduced to act in the catalytic reaction and only 5% of CBZ was

417 removed by the PMS system alone at 30 min. It meant that PMS was unable to be

418 activated when only PMS was present in the reaction system. While in CMB/PMS

419 system, CMB has a certain activation capacity for PMS, which might be attributed to

420 the fact that CMB contained functional groups such as semi-quinones which could be

421 involved in the reaction as redox ligands [50, 71]. Particularly, compared to the CMB

422 and Co@NPC systems under the appearance of PMS, the Co@NPC-CMB/PMS system

423 exhibited better degradation performance. Under the same conditions, the Co@NPC-

424 CMB/PMS system reached 100% CBZ in a much shorter time, which was greatly

425 improved compared to the previous system. On the one hand, the cow manure substrate

426 uniformly dispersed ZIF-67 precursor and effectively advanced the dispersion of

427 Co@NPC, avoiding the agglomeration phenomenon of Co particles that led to the

428 decrease of reaction active sites. The porous networks formed by the pyrolysis reaction

429 increased the contacting specific surface area of pollutant molecules and catalysts. On

430 the other hand, the unique electron structure of BC absorbed surrounding pollutant

431　molecules and accelerated charge transfer capability on catalysts [72]. It could

432　effectively increase the concentration of pollutants around the catalyst while also

433　accelerating electron migration and transformation on active sites [73]. Thus, the

434　synergistic effect between Co and biochar effectively improved the catalytic activity in

435　the Co@NPC-CMB/PMS system.

436　　　Fig. 5c reflected the dissolution of cobalt ions in different systems. The ICP-OES

437　results revealed that the Co content in Co@NPC-CMB was about 1.37 wt% after acid

438　etching, and the dissolved amounts in Co@NPC-CMB/PMS were much lower than that

439　in Co@NPC/PMS system. This was most probably due to the confinement and

440　protection provided by BC and graphitic carbon layers which prevented the leaching of

441　Co ions. Additionally, the catalysts that survived acid etching could effectively reduce

442　the Co leaching. The catalytic activity of Co@NPC-CMB was examined by measuring

443　the residual PMS concentration during the reaction (Fig. 5d). As the reaction progressed,

444　the concentration of PMS decreased continuously. After 30 minutes, the residual

445　concentration of PMS in the Co@NPC-CMB/PMS system decreased from 0.4 mM to

446　0.18 mM. In other words, the decomposition rate of PMS in the Co@NPC-CMB/PMS

447　system reached 55% which implied that Co@NPC-CMB had a high catalytic activity

448　for PMS.

3.3 Effect of parameters on catalytic activity of catalyst
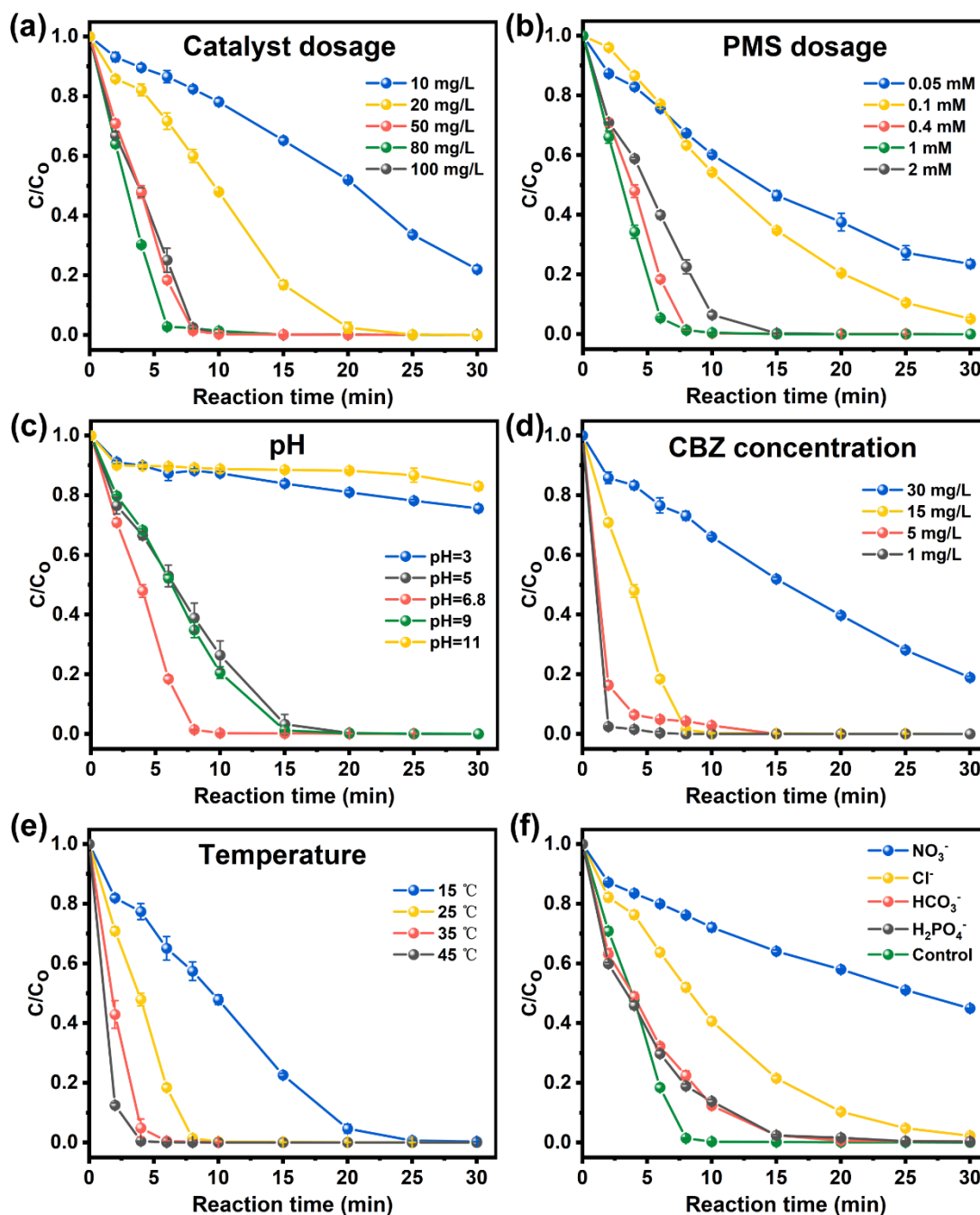
Fig. 6. The effect of different conditions of CBZ removal rate: (a) catalyst dosage, (b) PMS dosage, (c) initial solution pH, (d) initial concentration of CBZ, (e) temperature, (f) effects of inorganic anions. (experiment conditions: [CBZ] = 15 mg/L, [PMS] = 0.4 mM, [Co@NPC-CMB = 50 mg/L, pH = 6.8, T = 25 °C, When one parameter was changed, the remaining parameters remain unchanged).

Fig. 6 investigated the effects of different parameters (catalyst dosage, PMS dosage, initial pH, CBZ concentration, temperature and inorganic anions) on the degradation of

458 CBZ by the Co@NPC-CMB/PMS system. Fig. 6a demonstrated the influence of

459 catalyst dosage on the degradation efficiency of CBZ. It could be found that 89.5% of

460 CBZ was degraded within 30 min when the dosage of Co@NPC-CMB was 10 mg/L.

461 This result indicated that lower catalyst dosages could not provide sufficient reactive

462 sites for PMS. With the catalyst dosage increased from 10 mg/L to 80 mg/L, the CBZ

463 removal rate improved significantly and raised to 100% removal. It was because that

464 increasing amount of catalyst would lead to more active sites in the reaction system,

465 which was expected to produce more free radicals. Therefore, the system could achieve

466 complete degradation of CBZ in a short time. However, the degradation of CBZ

467 appeared to be inhibited as the catalyst dosage reached 100 mg/L. The corresponding

468 apparent reaction rate constant (k_{obs}) declined from 0.312 min^{-1} at 50 mg/L to 0.283

469 min^{-1} at 100 mg/L (Fig. S10a). The reason was that excessive catalysts would generate

470 a large number of free radicals transiently, leading to the self-quenching phenomenon

471 of radicals (Eq.(1-2)) [74]. As a result, inefficient consumption of excess PMS

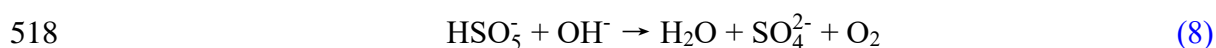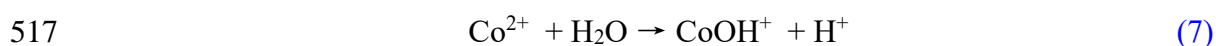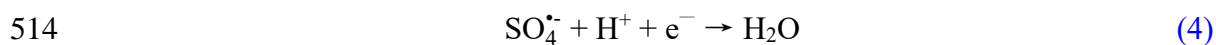472 prevented the catalytic reaction from progressing.

473 $$SO_4^{\bullet-} + SO_4^{\bullet-} \rightarrow S_2O_8^{2-} \tag{1}$$

474 $$SO_4^{\bullet-} + OH^{\bullet} \rightarrow HSO_5^- \tag{2}$$

475 PMS served as the source of reactive radicals such as $SO_4^{\bullet-}$ and $OH^{\bullet}$, which was

476 meant to explore the effect of the variation of PMS dosage on the reaction system. The

477 results in Fig. 6b showed that the removal of CBZ was 76.5% and 94.9% when using

478 0.05 mM and 0.1 mM PMS. When the PMS dosage was insufficient, it responded

479 quickly after a specific amount of catalyst was added. Adsorption was the only way for

480 the unreacted catalyst to remove CBZ. Thus, the unsatisfactory catalytic performance

481 was caused by the rapid consumption of inadequate PMS by the catalyst. Moreover, the

482 increase in PMS dosage from 0.1 mM to 1 mM resulted in a significantly increased

483 degradation rate of CBZ to 100%. It suggested that high PMS dosage accelerated the

484 production of free radicals at which point the number of free radicals might increase

485 with increasing dosage of PMS. However, further increasing the dosage inhibited the

486   progress of the catalytic reaction, and k_{obs} decreased to 0.368 min^{-1} when the PMS

487   dosage was 2 mM during the experiment (Fig. S10b). The possible explanation might

488   be the active sites on the catalyst surface have been saturated when the PMS dosage

489   reached a certain level, limiting the production of free radicals. In the meantime,

490   excessive PMS destroyed the pH of the solution causing self-quenching of free radicals.

491   Moreover, excess PMS might also react with free radicals to produce less reactive $SO_5^{\bullet-}$

492   (Eq.(3)) [75].

$$HSO_5^- + SO_4^{\bullet-} / OH^{\bullet} \rightarrow SO_5^{\bullet-} + SO_4^{2-} + H^+ / OH^- \tag{3}$$
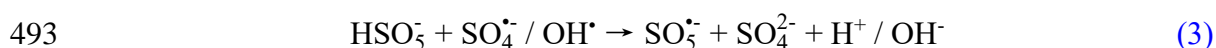
494   pH was considered to be a key factor in the reaction process of SR-AOPs,

495   influencing the type of free radicals produced and the charge state of the reactants [18].

496   Fig. 6c examined the effect of different initial pH (3-11) on the catalytic activity. Under

497   the conditions of unadjusted solution pH (pH=6.8) and weak acid/basic environment,

498   complete degradation of CBZ was achieved within 30 min. At pH values ranging from

499   5 to 9, the Co@NPC-CMB/PMS system demonstrated excellent catalytic performance.

500   However, only 24.4% of CBZ was removed when pH=3. Under strongly acidic

501   conditions with large amounts of H$^+$ in the reaction solution, the O-O bond of PMS was

502   broken and hydrogen bonds would be formed thus the radicals were consumed (Eq.(4-

503   5)) [63]. Simultaneously, such H$^+$ combined with $SO_4^{\bullet-}$ to form low activity $H_2SO_5^-$ to

504   inhibit the degradation reaction [76]. Likewise, the degradation of CBZ was strongly

505   inhibited under strongly alkaline conditions. $SO_4^{\bullet-}$ was replaced by OH$^{\bullet}$ which was

506   present in the solution when the pH value reached 11 (Eq.(6)). Since the standard

507   reduction potential of OH$^{\bullet}$ was lower than $SO_4^{\bullet-}$ and such a difference would reduce the

508   degradation of CBZ under alkaline conditions. On the other hand, the Co from the

509   catalyst surface would complex with OH$^{\bullet}$ to form less reactive CoOH$^+$ and self-

510   degradation of PMS would occur (Eq.(7-8)) [77, 78]. The production of sulphate

511   radicals was reduced greatly which further decreased the degradation efficiency of CBZ.

512   Overall, Co@NPC-CMB/PMS system has the best catalytic performance under neutral,

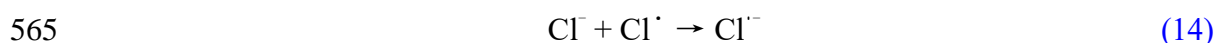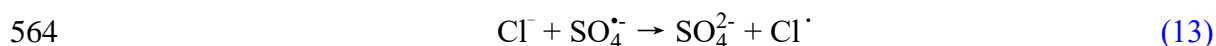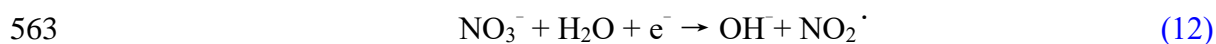513   weakly acidic and weakly basic conditions.

$$SO_4^{\bullet-} + H^+ + e^- \rightarrow H_2O \tag{4}$$

$$OH^\bullet + H^+ + e^- \rightarrow HSO_4^- \tag{5}$$

$$SO_4^{\bullet-} + OH^- \rightarrow SO_4^{2-} + OH^\bullet \tag{6}$$

$$Co^{2+} + H_2O \rightarrow CoOH^+ + H^+ \tag{7}$$

$$HSO_5^- + OH^- \rightarrow H_2O + SO_4^{2-} + O_2 \tag{8}$$

As shown in Fig. 6d, the effect of the initial CBZ concentration on the reaction was investigated by adjusting the pollutant model concentration. It was noticeable that the removal efficiency of CBZ decreased slightly as the initial concentration of CBZ was increased from 1 mg/L to 15 mg/L. But the entire CBZ was still removed within 15 min. However, only 81.1% of CBZ was removed when the concentration was further increased to 30 mg/L. This was attributed to the fact that the increased concentration of pollutants led to a concentration difference between free radicals and pollutant molecules which affected the degradation rate. Eventually led to the result that the active sites on the catalyst were insufficient for reaction.

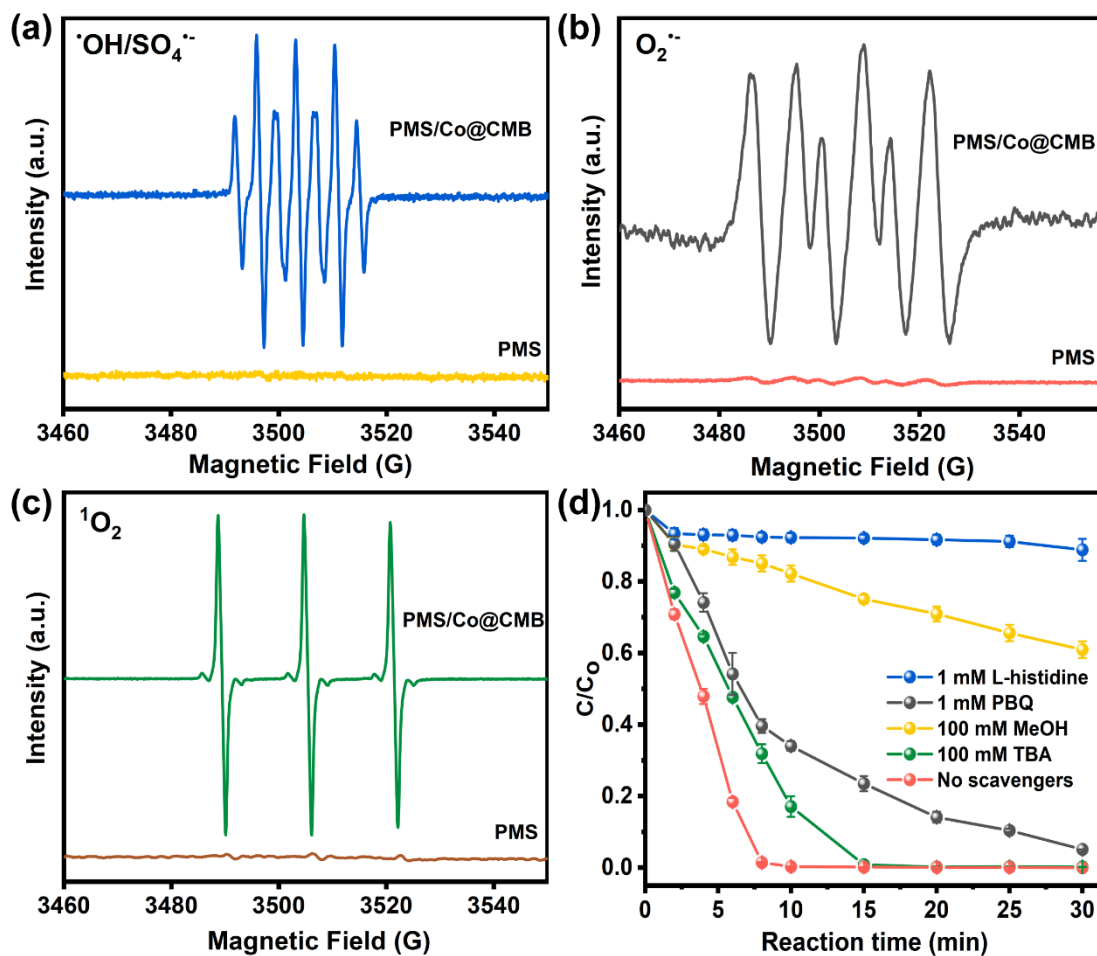The effect of the reaction temperature in the range of 15-45 °C on the Co@NPC-CMB/PMS system was assessed in Fig. 6e. The increasing reaction temperature would accelerate the diffusion rate of pollution molecules and the decomposition rate of PMS. It can be found that the degradation rate of CBZ accelerated significantly with increasing temperature. The results showed that k_{obs} raised from 0.202 min^{-1} to 1.065 min^{-1} as the temperature increased from 15 °C to 45 °C (Fig. S10e). The significant acceleration of the apparent reaction rate constant would likely be due to the increased reaction temperature, which speeded up the collision rate between reactants molecules. And the activation energy was calculated using the Arrhenius equation as given in Eq. (9) to be 39.38 KJ/mol (Fig. S11), where k was the apparent rate constant (min^{-1}), A was a pre-exponential factor, R was the universal gas constant (8.314 J·mol^{-1} K^{-1}), and T was the reaction temperature (K). Therefore, it could be known that the degradation of CBZ by the Co@NPC-CMB/PMS system was dependent on the intrinsic chemical reaction occurring on the catalyst surface [57]. And the increased temperature of the

542   reaction system would favor the production of more free radicals. Thus, the reaction

543   temperature had an important effect on the Co@NPC-CMB/PMS system.

544    $$ln\ k = ln\ A - E_a\ /\ RT \tag{9}$$

545   In practical aqueous environment applications, inorganic ions in water have

546   different degrees of influence on the reaction that catalyst activation of PMS to degrade

547   pollutants [79]. Therefore, inorganic anions (NO_3^-, Cl^-, HCO_3^-, $H_2PO_4^-$) were

548   introduced to investigate the degradation ability of the Co@NPC-CMB/PMS system in

549   a complex environment. Fig. 6f described the effect of inorganic anion in fixed

550   concentration (10 mM) on the catalytic reaction. It was discovered that the degradation

551   of CBZ was found to be significantly inhibited by 10 mM of NO_3^-. For this phenomenon,

552   it could be described as the reaction of NO_3^- with $SO_4^{\bullet-}$ and $OH^{\bullet}$ would produce the

553    $NO_3^{\bullet}$ and $NO_2^{\bullet}$ with low activity (Eq.(10-12)) [80]. Some of the radicals were

554   inefficiently consumed and then inhibited the catalytic reaction. Likewise, Cl^- inhibited

555   the degradation of CBZ with k_{obs} decreasing from 0.312 min^{-1} to 0.127 min^{-1} when the

556   Cl^- concentration increased from 0 mM to 10 mM (Fig. S10f). Yet the final degradation

557   rate still reached 97.7%. This might be explained by the fact that Cl^- could combine

558   with radicals to form less reactive chlorine radicals like $Cl^{\bullet}$ and $Cl_2^{\bullet-}$ (Eq.(13-14)) [81].

559   Additionally, a similar slight inhibition was observed for HCO_3^- and $H_2PO_4^-$, with k_{obs}

560   decreasing to 0.207 min^{-1} and 0.212 min^{-1}, respectively.

561    $$NO_3^- + SO_4^{\bullet-} \rightarrow SO_4^{2-} + NO_3^{\bullet} \tag{10}$$

562    $$NO_3^- + OH^{\bullet} \rightarrow OH^- + NO_3^{\bullet} \tag{11}$$

563    $$NO_3^- + H_2O + e^- \rightarrow OH^- + NO_2^{\bullet} \tag{12}$$

564    $$Cl^- + SO_4^{\bullet-} \rightarrow SO_4^{2-} + Cl^{\bullet} \tag{13}$$

565    $$Cl^- + Cl^{\bullet} \rightarrow Cl_2^{\bullet-} \tag{14}$$

3.4 Radical scavenging experiment

Fig. 7. (a)(b)(c) EPR spectra of DMPO and TEMP as the trapping agent, respectively. (d) Effects of different free radical scavengers on the degradation of CBZ in Co@NPC-CMB/PMS system. (experiment conditions: [CBZ] = 15 mg/L, [PMS] = 0.4 mM, [catalyst] = 50 mg/L, pH = 6.8, T = 25 °C).

EPR spectroscopy was used to identify the reactive radicals that may be present during the degradation of CBZ. According to previous reports, the activation of PMS was usually accompanied by the formation of $OH^\bullet$ and $SO_4^{\bullet-}$ [78]. DMPO was selected as a trapping agent for $SO_4^{\bullet-}$ and $OH^\bullet$ radicals. As shown in Fig. 7a, peaks were absent when the catalyst was not added, implying that $OH^\bullet$ and $SO_4^{\bullet-}$ would not be produced in lack of catalyst. However, with the addition of Co@NPC-CMB, no characteristic peaks belonging to $OH^\bullet$ and $SO_4^{\bullet-}$ appeared in the spectra. And the signal appeared as a clear seven-peaked signal ($\alpha N = 7.3 \pm 0.1$ G and $\alpha H = 3.9 \pm 0.1$ G) which was attributed to the hyperfine splitting of the oxidation product of DMPO, forming 5,5-

581   dimethylpyrrolidone-2-yloxy-(1) or 5,5-dimethyl-1-pyrrolidone-2-yloxy-(X) (DMPO-

582   X) [82]. The appearance of this phenomenon implied the presence of highly reactive

583   oxygen-containing molecules during the catalytic reaction, leading to the rapid

584   oxidation of DMPO. Thereby, DMPO opted as a spin trap for the capture of superoxide

585   radicals. And the typical quadruple characteristic peak signal of the DMPO-$O_2^{\bullet-}$ adduct

586   was observed in Fig. 7b which confirmed the appearance of free radicals in catalytic

587   reactions.

588   TEMP was introduced as a trapping agent to identify other active species which

589   may occur throughout the reaction. Singlet oxygen ($^1O_2$) was reported to be

590   demonstrated as a typical non-radical pathway for the degradation of contaminants in

591   SR-AOPs [68]. As illustrated in Fig. 7c, the high-intensity EPR spectral peak of triplet

592   state with the intensity ratio of 1:1:1 ($\alpha N = 16.9$ G) was observed in the presence of

593   both Co@NPC-CMB and PMS. It was consistent with the signal of the TEMP-$^1O_2$

594   adduct that certificated $^1O_2$ was present in the catalytic process. The spectrum clearly

595   displayed that the triplet peak was relatively weak in the absence of catalysts. While in

596   the Co@NPC-CMB/PMS system the signal of TEMP-$^1O_2$ was significantly enhanced

597   which demonstrated that Co@NPC-CMB could promote the self-quenching of PMS to

598   generate $^1O_2$.

599   For purpose of determining the contribution of reactive radicals during the catalytic

600   reaction and further investigating the activation mechanisms. Methanol, *tert*-butanol,

601   L-histidine and p-benzoquinone were used as quenchers to capture free radicals.

602   Methanol acted as the scavenger for $SO_4^{\bullet-}$ and OH$^\bullet$, TBA as the selective probe for OH$^\bullet$,

603   PBQ served to trap superoxide radicals and L-His was targeted to remove singlet

604   oxygen from the reaction system [74].

605   The results of the experiment by using scavengers were depicted in Fig. 7d.

606   Without adding any quencher, it was observed that CBZ was eliminated completely

607   within 10 minutes. When equal amounts (100 mM) of TBA and methanol were injected,

608   the former has a degradation rate of 99.8% while the latter reached 39%. Obviously, the

609   removal of CBZ was only slightly inhibited by TBA. In comparison, the inhibition

610   effect of MeOH was more significant than TBA. The phenomenon could be attributed

611   to the simultaneous production of $SO_4^{\cdot-}$ and $OH^{\cdot}$ during the activation of PMS, but the

612   contribution of $SO_4^{\cdot-}$ in the degradation process was more important as compared to $OH^{\cdot}$.

613   It also implied that other radical or non-radical pathways may be involved in the

614   degradation reaction. Therefore, 1 mM of PBQ was added and the clearance of CBZ

615   decreased to 83.9%. Apparently, the quenching effect of $O_2^{\cdot-}$ to the degrading efficiency

616   was quite limited as well. To further examine the contribution of the non-radical

617   pathway toward the reaction system, 1 mM of L-His was incorporated into the reaction

618   solution. The results implied that only 11.1% CBZ was removed in 30min, which

619   indicated that L-His had the most significant inhibition effect compared to other

620   quenchers. Based on the experimental results above, $^1O_2$ played a dominant role in the

621   degradation of CBZ by Co@NPC-CMB/PMS system. Typically, $^1O_2$ can be generated

622   by the self-quenching of PMS (Eq. (15)), and the catalyst could effectively accelerate

623   the self-quenching of PMS to produce more $^1O_2$. Additionally, the carbonaceous

624   catalyst mediated electron transfer through ketone groups also led to the production of

625    $^1O_2$. In summary, the free radical pathway and the non-radical pathway worked together

626   in the degradation of CBZ by the Co@NPC-CMB/PMS system. And $^1O_2$ played a major

627   role in the degradation reaction rather than the free radical pathway.

628
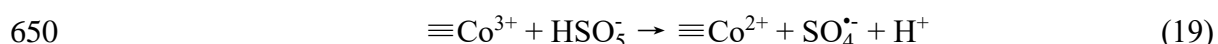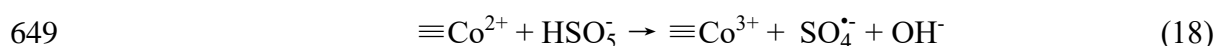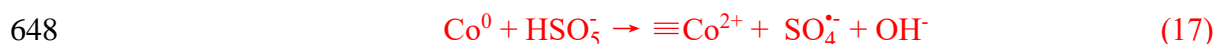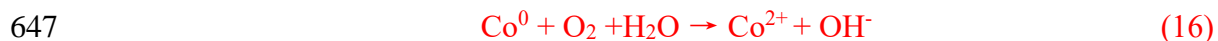$$HSO_5^- + SO_5^{2-} \rightarrow HSO_4^- + SO_4^{2-} + {}^1O_2 \tag{15}$$
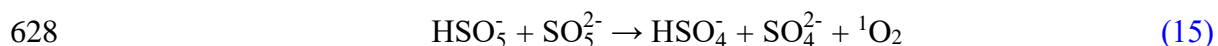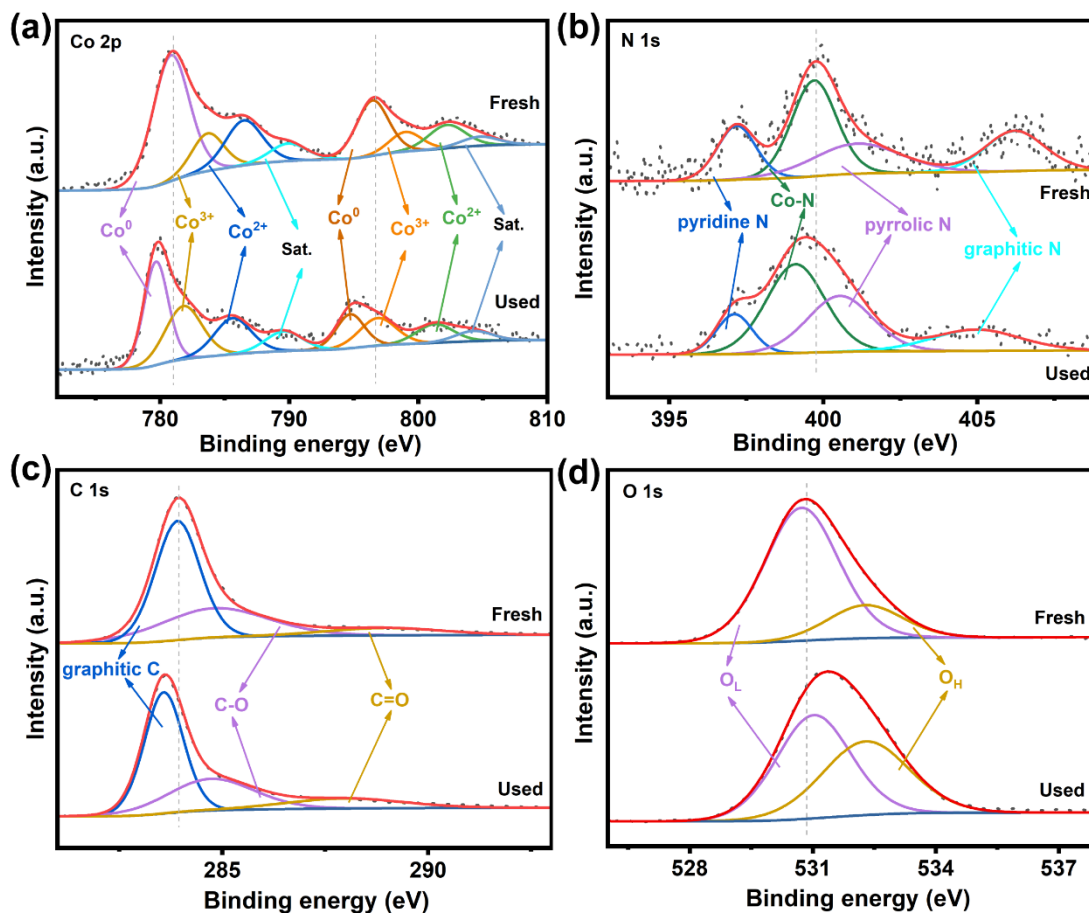
Fig. 8. XPS spectra of the Co@NPC-CMB: (a) Co 2p core level, (b) N 1s core level, (c) C 1s core level, (d) O 1s core level.

To further understand the mechanism of CBZ degradation by Co@NPC-CMB/PMS system, XPS was used to determine the changes in the chemical valence state of Co@NPC-CMB elements before and after the reaction. As shown in Fig. S12, characteristic peaks of C 1s, N 1s, O1s and Co 2p appeared in the survey XPS spectrum of both fresh and used samples, demonstrating the good stability of Co@NPC-CMB during the reaction.

In the Co 2p spectra in Fig. 8a, it was observed that the ratio of Co^{3+} increased from 21.58% to 37.95% accompanied by the decrease of Co^0 and Co^{2+} ratio after the catalytic reaction, which implied that Co underwent electron transfer during the reaction. In the process of activating PMS through Co@NPC-CMB, Co^0 can be oxidized to Co^{2+} in oxygenated water at first, or supplied electrons to PMS to produce $SO_4^{\cdot-}$ (Eq. (16-17)).

At the same time, the change in the chemical valence of Co from +2 to +3 occurred and Co^{3+} would continue to react with HSO_5^- to complete the redox cycle with the reaction formula as Eq. (18-19).

$$Co^0 + O_2 + H_2O \rightarrow Co^{2+} + OH^- \tag{16}$$

$$Co^0 + HSO_5^- \rightarrow \equiv Co^{2+} + SO_4^{\bullet-} + OH^- \tag{17}$$

$$\equiv Co^{2+} + HSO_5^- \rightarrow \equiv Co^{3+} + SO_4^{\bullet-} + OH^- \tag{18}$$

$$\equiv Co^{3+} + HSO_5^- \rightarrow \equiv Co^{2+} + SO_4^{\bullet-} + H^+ \tag{19}$$

Regarding N, N 1s can be divided into four peaks at 397.18 eV, 399.70eV, 401.10 eV, and 406.22 eV, which belong to pyridine N, Co-N, pyrrolic N and graphitic N, respectively (Fig. 8b) [83]. In general, pyridine N could facilitate electron transfer at the interface of carbon-based catalysts and the presence of graphitic N represented a good electron transfer capability. The relative content of pyridine N and graphite N decreased appreciably from 18.27% and 20.83% to 11.85 % and 15.42 % after activated PMS, which indicated that pyridine N and graphitic N played an important role in the electron transfer process within the Co@NPC-CMB/PMS system. Moreover, the Co-N bonds had a significant contribution to the activation of PMS which was attributed to the abundant free-pouring π-electrons of N-doped C [59]. Therefore, the N species played an important role in Co@NPC-CMB/PMS system.

Fig. 8c showed the C 1s spectra of fresh and used Co@NPC-CMB. Ketone groups have been proven to be reactive groups with a high electron content and hence have an excellent ability to activate PMS [84]. The decreased ratio of C=O and the increased C-O content accompanied the degradation reaction attributed to the involvement of C=O in the reaction of activated PMS to generate $^1O_2$, in which the oxygen-containing groups were transformed. In addition, the differences in the catalytic effectiveness of catalysts prepared at different pyrolysis temperatures were closely related to the structural role of graphitic C. This meant that the carbon structure was an important factor that influenced the catalytic reaction. It can be inferred that the graphite C structure and the ketone group play positive roles in the activation of PMS.

672   The high-resolution XPS spectra of O 1s were shown in Fig. 8d. The binding

673   energies with the two peaks were located at 530.75 eV and 532.3 eV derived from lattice

674   oxygen (O_L) and surface hydroxyl oxygen (O_H) species. After activation of PMS, the

675   relative content of O_H rose from 19.36% to 45.54% which may be due to the generation

676   of more hydroxyl compounds like Co-OH [18, 59]. According to previous reports, -OH

677   was an important reactive oxygen species to accelerate the charge transfer between the

678   active sites on the catalyst surface and PMS [85]. Normally, when the elements lost

679   electrons, the binding energy would shift to a higher value [66]. And the binding energy

680   of O 1s increased from 530.85 eV to 531.4 eV after the reaction which meant that part

681   of the electrons in oxygen functional groups was transferred from the Co@NPC-CMB

682   surface into PMS. It could be inferred that the oxygen functional group in Co@NPC-

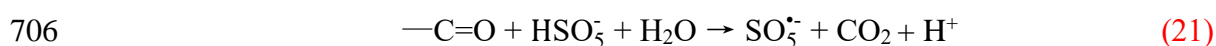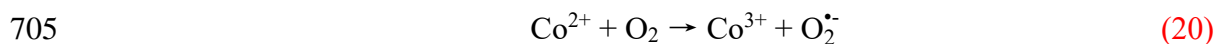683   CMB has a positive effect on the activation of PMS.
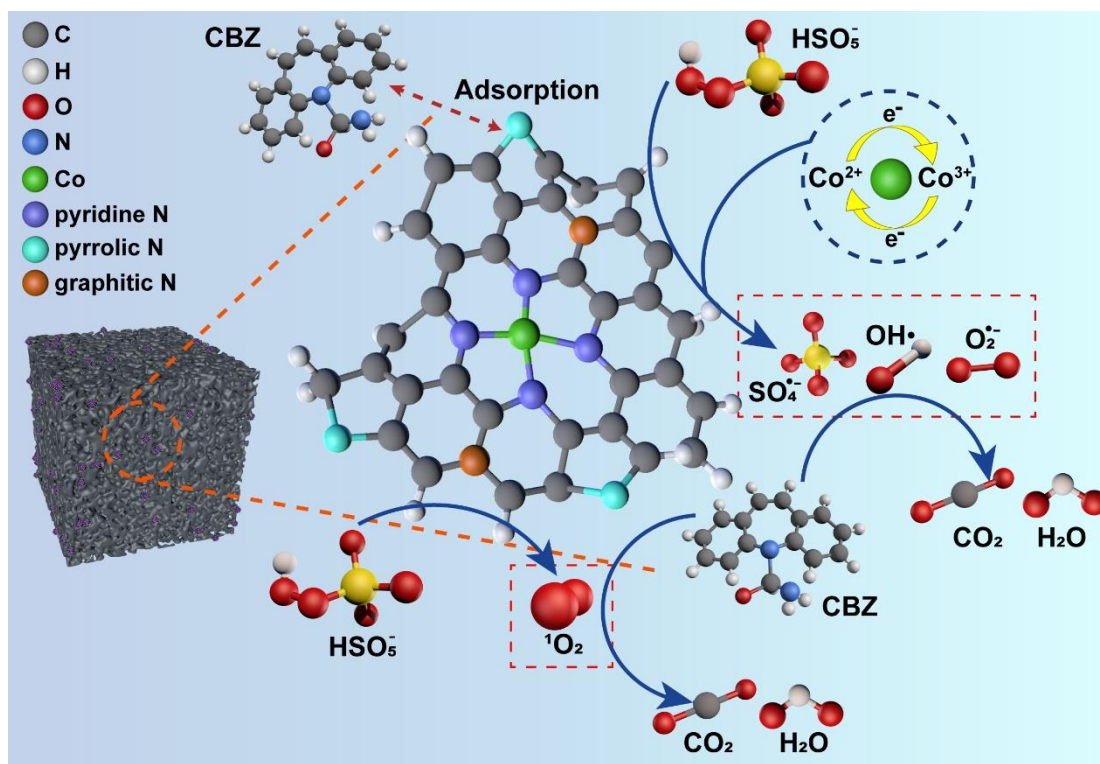
685 Fig. 9. The degradation mechanisms of CBZ in Co@NPC-CMB/PMS system.

686   Overall, based on the above results and previous studies, the possible mechanisms

687   that occurred during the activation of PMS by Co@NPC-CMB were proposed. Two

688   pathways were involved in the degradation of CBZ by the Co@NPC-CMB/PMS

689 system which were the free radical pathway and the non-free radical pathway. In the

690 free radical pathway, Co^{2+} has a valence change to provide electrons to PMS to generate

691 $SO_4^{\bullet-}$, $OH^{\bullet}$ and $O_2^{\bullet-}$ while itself was oxidized to Co^{3+} (Eq. (18) and (20)). Then Co^{3+}

692 continued to react with HSO_5^- and been reduced to Co^{2+} for the redox cycle (Eq. (19)).

693 According to the literature, the reductive functional groups in BC such as phenolic

694 hydroxyl groups could continue to act as reducing agents to promote the reduction of

695 transition metals [86]. It meant that the interaction between BC and transition metals

696 promoted the cyclic redox reaction. So that the catalyst can work continuously to

697 prolong the catalytic activity. In addition, the non-free radical pathway would occur

698 through the self-quenching of PMS. During the reaction, PMS was absorbed in active

699 sites on the catalyst surface, at which time the electrons on the catalyst surface tended

700 to approach and activate PMS [57]. Then those activated PMS were in contact with

701 each other and aggregated on the catalyst surface to form $^1O_2$ (Eq. (15)). At the same

702 time, the electron-rich C=O functional group could obtain electrons from PMS to form

703 SO_5^- and SO_5^- happened self-quenching to generate $^1O_2$ (Eq. (21-23)). Finally, 39% of

704 the pollutant molecules were mineralized as shown in Fig. S13.

705
$$Co^{2+} + O_2 \rightarrow Co^{3+} + O_2^{\bullet-} \tag{20}$$

706
$$-C=O + HSO_5^- + H_2O \rightarrow SO_5^{\bullet-} + CO_2 + H^+ \tag{21}$$

707
$$SO_5^{\bullet-} + SO_5^{\bullet-} \rightarrow S_2O_8^{2-} + {}^1O_2 \tag{22}$$

708
$$SO_5^{\bullet-} + SO_5^{\bullet-} \rightarrow SO_4^{2-} + {}^1O_2 \tag{23}$$

709   *3.6. Reusability and stability of Co@NPC-CMB*

710   The stability and reusability of Co@NPC-CMB were evaluated by catalytic

711   recycling measurements. The used catalyst was collected, washed with pure water and

712   dried, and then put into the experiment under the same condition. The results were

713   shown in Fig. S14, Co@NPC-CMB gradually lost its catalytic activity after four cycles.

714   About 50% of the CBZ was degraded, and the reduction in catalytic activity may be

715   caused by the coating of intermediate products on the catalyst surface and changing in

716   active sites during the reaction process. According to previous reports, heating

717   treatment could remove the intermediate products which adsorbed on the catalyst

718   surface [87]. Then the Co@NPC-CMB was heated at 350 ℃ after four-cycle use and

719   the degradation experiments were continued. However, after the heating treatment, the

720   CBZ removal efficiency reached 87.5% which meant that the heating treatment

721   effectively restored the catalytic activity of catalysts. Fig. S15 showed SEM images of

722   the Co@NPC-CMB after four-cycle. It can be seen that the catalyst surface still retained

723   the porous structure and the hexahedral structure of ZIF-67 precursor was unbroken

724   (Fig. S15b). The structural integrity and the encapsulation of the surface carbon layers

725   might effectively protect the active sites and maintain the stability of Co@NPC-CMB.

4. Conclusion

In this paper, Co@NPC-CMB-x biochar-based catalysts were successfully prepared by pyrolysis method using cow dung as raw material. The influence of pyrolysis temperature on the intrinsic performance and catalytic effect of Co@NPC-CMB-x was explored, and systematically investigated the effect on the activation of PMS for the CBZ degradation by Co@NPC-CMB-x. The results showed that Co@NPC-CMB-800 has higher crystallinity and more graphite degree which provided abundant active sites. It showed excellent degradation performance almost all CBZ (15 mg/L) was removed within 30min and adapted to the range of pH conditions (5-9). XPS results showed that the biochar substrate had good catalytic activity in the Co/PMS system and accelerated the redox cycle of Co^{2+}/Co^{3+}. Meanwhile, based on the elucidation of the radical/non-radical synergistic catalytic mechanism, the reaction mechanism of Co@NPC-CMB/PMS for the degradation of CBZ was proposed, revealing that $^1O_2$ was the dominant active species for pollutant degradation. This work converted livestock industry waste cow manure into the support of transition metals and provided a new idea for the application of biochar-based materials in sewage treatment.

Conflict of Interest

The authors have no conflicts of interest to declare.

References:

[1] C.G. Otoni, H.M.C. Azeredo, B.D. Mattos, M. Beaumont, D.S. Correa, O.J. Rojas, The Food-Materials Nexus: Next Generation Bioplastics and Advanced Materials from Agri-Food Residues, Adv. Mater., (2021) 2102520.

[2] C. Zhao, B. Shao, M. Yan, Z. Liu, Q. Liang, Q. He, T. Wu, Y. Liu, Y. Pan, J. Huang, J. Wang, J. Liang, L. Tang, Activation of peroxymonosulfate by biochar-based catalysts and applications in the degradation of organic contaminants: A review, Chem. Eng. J., 416 (2021) 128829.

[3] G. Prasannamedha, P.S. Kumar, R. Mehala, T.J. Sharumitha, D. Surendhar, Enhanced adsorptive removal of sulfamethoxazole from water using biochar derived from hydrothermal carbonization of sugarcane bagasse, J. Hazard. Mater., 407 (2021) 124825.

[4] C.E. Brewer, R. Unger, K. Schmidt-Rohr, R.C. Brown, Criteria to Select Biochars for Field Studies based on Biochar Chemical Properties, BioEnergy Research, 4 (2011) 312-323.

[5] R.Y. Shi, Z.N. Hong, J.Y. Li, J. Jiang, M.A. Kamran, R.K. Xu, W. Qian, Peanut straw biochar increases the resistance of two Ultisols derived from different parent materials to acidification: A mechanism study, J. Environ. Manage., 210 (2018) 171-179.

[6] S. Ye, G. Zeng, X. Tan, H. Wu, J. Liang, B. Song, N. Tang, P. Zhang, Y. Yang, Q. Chen, X. Li, Nitrogen-doped biochar fiber with graphitization from Boehmeria nivea for promoted peroxymonosulfate activation and non-radical degradation pathways with enhancing electron transfer, Appl. Catal. B, 269 (2020) 118850.

[7] X. Xiong, I.K.M. Yu, L. Cao, D.C.W. Tsang, S. Zhang, Y.S. Ok, A review of biochar-based catalysts for chemical synthesis, biofuel production, and pollution control, Bioresour. Technol., 246 (2017) 254-270.

[8] P. Zhang, Y. Li, Y. Cao, L. Han, Characteristics of tetracycline adsorption by cow manure biochar prepared at different pyrolysis temperatures, Bioresour. Technol., 285 (2019) 121348.

[9] H. Li, R. Qu, C. Li, W. Guo, X. Han, F. He, Y. Ma, B. Xing, Selective removal of polycyclic aromatic hydrocarbons (PAHs) from soil washing effluents using biochars produced at different pyrolytic temperatures, Bioresour. Technol., 163 (2014) 193-198.

[10] V. Hansen, D. Müller-Stöver, L.J. Munkholm, C. Peltre, H. Hauggaard-Nielsen, L.S. Jensen, The effect of straw and wood gasification biochar on carbon sequestration, selected soil fertility indicators and functional groups in soil: An incubation study, Geoderma, 269 (2016) 99-107.

[11] J. Xiao, R. Hu, G. Chen, Micro-nano-engineered nitrogenous bone biochar developed with a ball-milling technique for high-efficiency removal of aquatic Cd(II), Cu(II) and Pb(II), J. Hazard. Mater., 387 (2020) 121980.

[12] C. Peiris, S.R. Gunatilake, T.E. Mlsna, D. Mohan, M. Vithanage, Biochar based removal of antibiotic sulfonamides and tetracyclines in aquatic environments: A critical review, Bioresour. Technol., 246 (2017) 150-159.

[13] J. Iqbal, N.S. Shah, M. Sayed, N.K. Niazi, M. Imran, J.A. Khan, Z.U.H. Khan, A.G.S. Hussien, K. Polychronopoulou, F. Howari, Nano-zerovalent manganese/biochar

composite for the adsorptive and oxidative removal of Congo-red dye from aqueous solutions, J. Hazard. Mater., 403 (2021) 123854.

[14] K.C. Uzoma, M. Inoue, H. Andry, H. Fujimaki, A. Zahoor, E. Nishihara, Effect of cow manure biochar on maize productivity under sandy soil condition, Soil Use Manag., 27 (2011) 205-212.

[15] Y. Zhang, S.U. Geissen, C. Gal, Carbamazepine and diclofenac: removal in wastewater treatment plants and occurrence in water bodies, Chemosphere, 73 (2008) 1151-1161.

[16] B. Kasprzyk-Hordern, R.M. Dinsdale, A.J. Guwy, The occurrence of pharmaceuticals, personal care products, endocrine disruptors and illicit drugs in surface water in South Wales, UK, Water Res., 42 (2008) 3498-3518.

[17] H. Zeng, L. Deng, Z. Shi, J. Luo, J. Crittenden, Heterogeneous degradation of carbamazepine by Prussian blue analogues in the interlayers of layered double hydroxides: performance, mechanism and toxicity evaluation, J. Mater. Chem. A, 7 (2019) 342-352.

[18] Q.-T. Sun, B.-D. Xu, J. Yang, T.-T. Qian, H. Jiang, Layered oxides supported Co-Fe bimetal catalyst for carbamazepine degradation via the catalytic activation of peroxymonosulfate, Chem. Eng. J., 400 (2020) 125899.

[19] C.M. Dai, S.U. Geissen, Y.L. Zhang, Y.J. Zhang, X.F. Zhou, Performance evaluation and application of molecularly imprinted polymer for separation of carbamazepine in aqueous solution, J. Hazard. Mater., 184 (2010) 156-163.

[20] J. Deng, Y.-q. Cheng, Y.-a. Lu, J.C. Crittenden, S.-q. Zhou, N.-y. Gao, J. Li, Mesoporous manganese Cobaltite nanocages as effective and reusable heterogeneous peroxymonosulfate activators for Carbamazepine degradation, Chem. Eng. J., 330 (2017) 505-517.

[21] S. Dong, L. Cui, Y. Tian, L. Xia, Y. Wu, J. Yu, D.M. Bagley, J. Sun, M. Fan, A novel and high-performance double Z-scheme photocatalyst ZnO-SnO_2-Zn_2SnO_4 for effective removal of the biological toxicity of antibiotics, J. Hazard. Mater., 399 (2020) 123017.

[22] J. Xiong, X. Li, J. Huang, X. Gao, Z. Chen, J. Liu, H. Li, B. Kang, W. Yao, Y. Zhu, CN/rGO@BPQDs high-low junctions with stretching spatial charge separation ability for photocatalytic degradation and H_2O_2 production, Appl. Catal. B, 266 (2020) 118602.

[23] K. Wei, A. Armutlulu, Y. Wang, G. Yao, R. Xie, B. Lai, Visible-light-driven removal of atrazine by durable hollow core-shell TiO_2@$LaFeO_3$ heterojunction coupling with peroxymonosulfate via enhanced electron-transfer, Appl. Catal. B, 303 (2022) 117795.

[24] X. Li, L. Ye, Z. Ye, S. Xie, Y. Qiu, F. Liao, C. Lin, M. Liu, N, P co-doped core/shell porous carbon as a highly efficient peroxymonosulfate activator for phenol degradation, Sep. Purif. Technol., 276 (2021) 119286.

[25] X. Duan, J. Kang, W. Tian, H. Zhang, S.-H. Ho, Y.-A. Zhu, Z. Ao, H. Sun, S. Wang, Interfacial-engineered cobalt@carbon hybrids for synergistically boosted evolution of sulfate radicals toward green oxidation, Appl. Catal. B, 256 (2019) 117795.

[26] B.C. Hodges, E.L. Cates, J.H. Kim, Challenges and prospects of advanced oxidation water treatment processes using catalytic nanomaterials, Nat. Nanotechnol.,

13 (2018) 642-650.

[27] Y. Liu, R. Luo, Y. Li, J. Qi, C. Wang, J. Li, X. Sun, L. Wang, Sandwich-like Co_3O_4/MXene composite with enhanced catalytic performance for Bisphenol A degradation, Chem. Eng. J., 347 (2018) 731-740.

[28] W. Ren, J. Gao, C. Lei, Y. Xie, Y. Cai, Q. Ni, J. Yao, Recyclable metal-organic framework/cellulose aerogels for activating peroxymonosulfate to degrade organic pollutants, Chem. Eng. J., 349 (2018) 766-774.

[29] J. Lim, J.M. Lee, C. Kim, S.-J. Hwang, J. Lee, W. Choi, Two-dimensional RuO_2 nanosheets as robust catalysts for peroxymonosulfate activation, Environ. Sci. Nano, 6 (2019) 2084-2093.

[30] Y. Lv, Y. Liu, J. Wei, M. Li, D. Xu, B. Lai, Bisphenol S degradation by visible light assisted peroxymonosulfate process based on $BiOI/B_4C$ photocatalysts with Z-scheme heterojunction, Chem. Eng. J., 417 (2021) 129188.

[31] I. Arslan-Alaton, T. Olmez-Hanci, G. Korkmaz, C. Sahin, Removal of iopamidol, an iodinated X-ray contrast medium, by zero-valent aluminum-activated H_2O_2 and $S_2O_8^{2-}$, Chem. Eng. J., 318 (2017) 64-75.

[32] X. Sun, H. Qi, S. Mao, Z. Sun, Atrazine removal by peroxymonosulfate activated with magnetic CoFe alloy@N-doped graphitic carbon encapsulated in chitosan carbonized microspheres, Chem. Eng. J., 423 (2021) 130169.

[33] C. Gong, F. Chen, Q. Yang, K. Luo, F. Yao, S. Wang, X. Wang, J. Wu, X. Li, D. Wang, G. Zeng, Heterogeneous activation of peroxymonosulfate by Fe-Co layered doubled hydroxide for efficient catalytic degradation of Rhoadmine B, Chem. Eng. J., 321 (2017) 222-232.

[34] M. Ding, X. Cai, H.L. Jiang, Improving MOF stability: approaches and applications, Chem Sci, 10 (2019) 10209-10230.

[35] Y. Qian, F. Zhang, H. Pang, A Review of MOFs and Their Composites‐Based Photocatalysts: Synthesis and Applications, Adv. Funct. Mater., 31 (2021) 2104231.

[36] X. Fang, B. Zong, S. Mao, Metal-Organic Framework-Based Sensors for Environmental Contaminant Sensing, Nanomicro Lett, 10 (2018) 64.

[37] D. Wang, Z. Liang, S. Gao, C. Qu, R. Zou, Metal-organic framework-based materials for hybrid supercapacitor application, Coord. Chem. Rev., 404 (2020) 213093.

[38] C. Fang, Z. Deng, G. Cao, Q. Chu, Y. Wu, X. Li, X. Peng, G. Han, Co–Ferrocene MOF/Glucose Oxidase as Cascade Nanozyme for Effective Tumor Therapy, Advanced Functional Materials, 30 (2020) 1910085.

[39] V.V. Butova, V.A. Polyakov, A.P. Budnyk, A.M. Aboraia, E.A. Bulanova, A.A. Guda, E.A. Reshetnikova, Y.S. Podkovyrina, C. Lamberti, A.V. Soldatov, Zn/Co ZIF family: MW synthesis, characterization and stability upon halogen sorption, Polyhedron, 154 (2018) 457-464.

[40] A. Phan, C.J. Doonan, F.J. Uribe-Romo, C.B. Knobler, M. O'Keeffe, O.M. Yaghi, Synthesis, Structure, and Carbon Dioxide Capture Properties of Zeolitic Imidazolate Frameworks, Acc. Chem. Res., 43 (2010) 58-67.

[41] K.S. Park, Z. Ni, A.P. Côté, J.Y. Choi, R. Huang, F.J. Uribe-Romo, H.K. Chae, M. O'Keeffe, O.M. Yaghi, Exceptional chemical and thermal stability of zeolitic imidazolate frameworks, Proc. Natl. Acad. Sci., 103 (2006) 10186-10191.

[42] R. Banerjee, B.W. A. Phan, C. Knobler, H. Furukawa, M. O'Keeffe, O.M. Yaghi, High-Throughput Synthesis of Zeolitic Imidazolate Frameworks and Application to CO_2 Capture, Science, 319 (2008) 939-943.

[43] W. Ma, N. Wang, Y. Fan, T. Tong, X. Han, Y. Du, Non-radical-dominated catalytic degradation of bisphenol A by ZIF-67 derived nitrogen-doped carbon nanotubes frameworks in the presence of peroxymonosulfate, Chem. Eng. J., 336 (2018) 721-731.

[44] J. Ye, J. Dai, C. Li, Y. Yan, Lawn-like Co_3O_4@N-doped carbon-based catalytic self-cleaning membrane with peroxymonosulfate activation: A highly efficient singlet oxygen dominated process for sulfamethoxazole degradation, Chem. Eng. J., 421 (2021) 127805.

[45] X. Zhang, G. Ji, W. Liu, B. Quan, X. Liang, C. Shang, Y. Cheng, Y. Du, Thermal conversion of an Fe_3O_4@metal-organic framework: a new method for an efficient Fe-Co/nanoporous carbon microwave absorbing material, Nanoscale, 7 (2015) 12932-12942.

[46] X. Li, C. Zeng, J. Jiang, L. Ai, Magnetic cobalt nanoparticles embedded in hierarchically porous nitrogen-doped carbon frameworks for highly efficient and well-recyclable catalysis, J. Mater. Chem. A, 4 (2016) 7476-7482.

[47] R. Li, J.J. Wang, L.A. Gaston, B. Zhou, M. Li, R. Xiao, Q. Wang, Z. Zhang, H. Huang, W. Liang, H. Huang, X. Zhang, An overview of carbothermal synthesis of metal–biochar composites for the removal of oxyanion contaminants from aqueous solution, Carbon, 129 (2018) 674-687.

[48] M.T. Yang, Y. Du, W.C. Tong, A.C.K. Yip, K.A. Lin, Cobalt-impregnated biochar produced from CO_2-mediated pyrolysis of Co/lignin as an enhanced catalyst for activating peroxymonosulfate to degrade acetaminophen, Chemosphere, 226 (2019) 924-933.

[49] L. Hu, R. Xiao, X. Wang, X. Wang, C. Wang, J. Wen, W. Gu, C. Zhu, MXene-induced electronic optimization of metal-organic framework-derived CoFe LDH nanosheet arrays for efficient oxygen evolution, Appl. Catal. B, 298 (2021) 120599.

[50] H. Xu, Y. Zhang, J. Li, Q. Hao, X. Li, F. Liu, Heterogeneous activation of peroxymonosulfate by a biochar-supported Co_3O_4 composite for efficient degradation of chloramphenicols, Environ. Pollut., 257 (2020) 113610.

[51] L. Li, C. Lai, F. Huang, M. Cheng, G. Zeng, D. Huang, B. Li, S. Liu, M. Zhang, L. Qin, M. Li, J. He, Y. Zhang, L. Chen, Degradation of naphthalene with magnetic bio-char activate hydrogen peroxide: Synergism of bio-char and Fe-Mn binary oxides, Water Res., 160 (2019) 238-248.

[52] X.L. Chen, F. Li, M. Zhang, B. Liu, H. Chen, H. Wang, Highly dispersed and stabilized Co_3O_4/C anchored on porous biochar for bisphenol A degradation by sulfate radical advanced oxidation process, Sci. Total Environ., 777 (2021) 145794.

[53] C. Liang, C.F. Huang, N. Mohanty, R.M. Kurakalva, A rapid spectrophotometric determination of persulfate anion in ISCO, Chemosphere, 73 (2008) 1540-1543.

[54] J. Di, M. Zhu, R. Jamakanga, X. Gai, Y. Li, R. Yang, Electrochemical activation combined with advanced oxidation on $NiCo_2O_4$ nanoarray electrode for decomposition of Rhodamine B, J. Water Process Eng., 37 (2020) 101386.

[55] Y. Liu, X. Chen, Y. Yang, Y. Feng, D. Wu, S. Mao, Activation of persulfate with

metal–organic framework-derived nitrogen-doped porous Co@C nanoboxes for highly efficient p-Chloroaniline removal, Chem. Eng. J., 358 (2019) 408-418.

[56] Z. Wang, X. Ke, K. Zhou, X. Xu, Y. Jin, H. Wang, M. Sui, Engineering the structure of ZIF-derived catalysts by revealing the critical role of temperature for enhanced oxygen reduction reaction, J. Mater. Chem. A, 9 (2021) 18515-18525.

[57] J. You, C. Zhang, Z. Wu, Z. Ao, W. Sun, Z. Xiong, S. Su, G. Yao, B. Lai, N-doped graphite encapsulated metal nanoparticles catalyst for removal of Bisphenol A via activation of peroxymonosulfate: A singlet oxygen-dominated oxidation process, Chem. Eng. J., 415 (2021) 128890.

[58] C. Sun, T. Chen, Q. Huang, M. Zhan, X. Li, J. Yan, Activation of persulfate by CO_2-activated biochar for improved phenolic pollutant degradation: Performance and mechanism, Chem. Eng. J., 380 (2020) 122519.

[59] Y. Zhou, Y. Zhang, X. Hu, Novel zero-valent Co-Fe encapsulated in nitrogen-doped porous carbon nanocomposites derived from $CoFe_2O_4$@ZIF-67 for boosting 4-chlorophenol removal via coupling peroxymonosulfate, J. Colloid Interface Sci., 575 (2020) 206-219.

[60] D. Ding, S. Yang, L. Chen, T. Cai, Degradation of norfloxacin by CoFe alloy nanoparticles encapsulated in nitrogen doped graphitic carbon (CoFe@N-GC) activated peroxymonosulfate, Chem. Eng. J., 392 (2020) 123725.

[61] L. Xie, G. Sun, F. Su, X. Guo, Q. Kong, X. Li, X. Huang, L. Wan, W. song, K. Li, C. Lv, C.-M. Chen, Hierarchical porous carbon microtubes derived from willow catkins for supercapacitor applications, J. Mater. Chem. A, 4 (2016) 1637-1646.

[62] X. Zhang, K. Zhang, H. Li, Q. Wang, L.e. Jin, Q. Cao, Synthesis of porous graphitic carbon from biomass by one-step method And its role in the electrode for supercapacitor, J. Appl. Electrochem., 48 (2018) 415-426.

[63] J. Luo, S. Bo, Y. Qin, Q. An, Z. Xiao, S. Zhai, Transforming goat manure into surface-loaded cobalt/biochar as PMS activator for highly efficient ciprofloxacin degradation, Chem. Eng. J., 395 (2020) 125063.

[64] Z. Wu, Z. Xiong, R. Liu, C. He, Y. Liu, Z. Pan, G. Yao, B. Lai, Pivotal roles of N-doped carbon shell and hollow structure in nanoreactor with spatial confined Co species in peroxymonosulfate activation: Obstructing metal leaching and enhancing catalytic stability, J. Hazard. Mater., 427 (2022) 128204.

[65] Y. Li, S. Ma, S. Xu, H. Fu, Z. Li, K. Li, K. Sheng, J. Du, X. Lu, X. Li, S. Liu, Novel magnetic biochar as an activator for peroxymonosulfate to degrade bisphenol A: Emphasizing the synergistic effect between graphitized structure and $CoFe_2O_4$, Chem. Eng. J., 387 (2020) 124094.

[66] X. Zhang, Y. Yang, H. Hao Ngo, W. Guo, F. Sun, X. Wang, J. Zhang, T. Long, Urea removal in reclaimed water used for ultrapure water production by spent coffee biochar/granular activated carbon activating peroxymonosulfate and peroxydisulfate, Bioresour. Technol., 343 (2022) 126062.

[67] Y. Gao, Y. Zhu, Z. Chen, C. Hu, Nitrogen-Coordinated Cobalt Embedded in a Hollow Carbon Polyhedron for Superior Catalytic Oxidation of Organic Contaminants with Peroxymonosulfate, Environ. Sci. Technol., 1 (2020) 76-85.

[68] Y. Wang, Y. Song, N. Li, W. Liu, B. Yan, Y. Yu, L. Liang, G. Chen, L. Hou, S.

Wang, Tunable active sites on biogas digestate derived biochar for sulfanilamide degradation by peroxymonosulfate activation, J. Hazard. Mater., 421 (2022) 126794.

[69] G.P. Anipsitakis, D.D. Dionysiou, Radical Generation by the Interaction of Transition Metals with Common Oxidants, Environ. Sci. Technol., 38 (2004) 3705-3712.

[70] W. Li, S. Li, Y. Tang, X. Yang, W. Zhang, X. Zhang, H. Chai, Y. Huang, Highly efficient activation of peroxymonosulfate by cobalt sulfide hollow nanospheres for fast ciprofloxacin degradation, J. Hazard. Mater., 389 (2020) 121856.

[71] R. Zhang, R. Zhang, R. Jian, L. Zhang, M.T. Zhang, Y. Xia, S. Luo, Bio-inspired lanthanum-ortho-quinone catalysis for aerobic alcohol oxidation: semi-quinone anionic radical as redox ligand, Nat. Commun., 13 (2022) 428.

[72] X. Cui, S.-S. Zhang, Y. Geng, J. Zhen, J. Zhan, C. Cao, S.-Q. Ni, Synergistic catalysis by Fe_3O_4-biochar/peroxymonosulfate system for the removal of bisphenol a, Sep. Purif. Technol., 276 (2021) 119351.

[73] J.R.J. Zaeni, J.-W. Lim, Z. Wang, D. Ding, Y.-S. Chua, S.-L. Ng, W.-D. Oh, In situ nitrogen functionalization of biochar via one-pot synthesis for catalytic peroxymonosulfate activation: Characteristics and performance studies, Sep. Purif. Technol., 241 (2020) 116702.

[74] Y. Lei, W. Sun, S.K. Tiwari, K. Thummavichai, O. Ola, X. Qin, Z. Ma, N. Wang, Y. Zhu, Zn/Co-ZIF reinforced sugarcane bagasse aerogel for highly efficient catalytic activation of peroxymonosulfate, J. Environ. Chem. Eng., 9 (2021) 106885.

[75] M. Ding, W. Ao, H. Xu, W. Chen, L. Tao, Z. Shen, H. Liu, C. Lu, Z. Xie, Facile construction of dual heterojunction $CoO@TiO_2$/MXene hybrid with efficient and stable catalytic activity for phenol degradation with peroxymonosulfate under visible light irradiation, J. Hazard. Mater., 420 (2021) 126686.

[76] C. Chen, M. Xie, L. Kong, W. Lu, Z. Feng, J. Zhan, Mn_3O_4 nanodots loaded g-C_3N_4 nanosheets for catalytic membrane degradation of organic contaminants, J. Hazard. Mater., 390 (2020) 122146.

[77] Z. Wu, Y. Wang, Z. Xiong, Z. Ao, S. Pu, G. Yao, B. Lai, Core-shell magnetic Fe_3O_4@Zn/Co-ZIFs to activate peroxymonosulfate for highly efficient degradation of carbamazepine, Appl. Catal. B, 277 (2020) 119136.

[78] Y. Yan, H. Zhang, W. Wang, W. Li, Y. Ren, X. Li, Synthesis of Fe(0)/Fe_3O_4@porous carbon through a facile heat treatment of iron-containing candle soots for peroxymonosulfate activation and efficient degradation of sulfamethoxazole, J. Hazard. Mater., 411 (2021) 124952.

[79] Y. Yang, Y. Li, P. Hong, Z. Wu, C. Xie, K. Zhang, L. Lianxiang, J. He, L. Kong, J. Liu, Surface-active MnFeO@C cubes as enhanced peroxymonosulfate activators for efficient degradation of bisphenol A, Appl. Surf. Sci., 538 (2021) 148008.

[80] Y. Ma, D. Xiong, X. Lv, X. Zhao, C. Meng, H. Xie, Z. Zhang, Rapid and long-lasting acceleration of zero-valent iron nanoparticles@Ti_3C_2-based MXene/peroxymonosulfate oxidation with bi-active centers toward ranitidine removal, J. Mater. Chem. A, 9 (2021) 19817-19833.

[81] D. Sun, C. Li, S. Lu, Q. Yang, C. He, Magnetic Fe_3O_4@CoFe-LDH nanocomposite heterogeneously activated peroxymonosulfate for degradation of azo-dye AO7, RSC

Adv., 11 (2021) 20258-20267.

[82] H. Fu, S. Ma, P. Zhao, S. Xu, S. Zhan, Activation of peroxymonosulfate by graphitized hierarchical porous biochar and $MnFe_2O_4$ magnetic nanoarchitecture for organic pollutants degradation: Structure dependence and mechanism, Chem. Eng. J., 360 (2019) 157-170.

[83] S. Lai, L. Xu, H. Liu, S. Chen, R. Cai, L. Zhang, W. Theis, J. Sun, D. Yang, X. Zhao, Controllable synthesis of CoN_3 catalysts derived from Co/Zn-ZIF-67 for electrocatalytic oxygen reduction in acidic electrolytes, J. Mater. Chem. A, 7 (2019) 21884-21891.

[84] M. Wang, H. Xu, Q. Li, G. Zhou, Q. Ye, Q. Wang, J. Zhang, Panda manure biochar-based green catalyst to remove organic pollutants by activating peroxymonosulfate: Important role of non-free radical pathways, J. Environ. Chem. Eng., 9 (2021) 106485.

[85] M. Ding, W. Chen, H. Xu, Z. Shen, T. Lin, K. Hu, C.H. Lu, Z. Xie, Novel alpha-Fe_2O_3/MXene nanocomposite as heterogeneous activator of peroxymonosulfate for the degradation of salicylic acid, J. Hazard. Mater., 382 (2020) 121064.

[86] M. Xu, J. Deng, A. Cai, C. Ye, X. Ma, Q. Li, S. Zhou, X. Li, Synergistic effects of UVC and oxidants (PS vs. Chlorine) on carbamazepine attenuation: Mechanism, pathways, DBPs yield and toxicity assessment, Chem. Eng. J., 413 (2021) 127533.

[87] T. Liu, K. Cui, Y. Chen, C. Li, M. Cui, H. Yao, Y. Chen, S. Wang, Removal of chlorophenols in the aquatic environment by activation of peroxymonosulfate with nMnOx@Biochar hybrid composites: Performance and mechanism, Chemosphere, 283 (2021) 131188.